Molecular origins of genome instability following a single chromosome mis-segregation event

Giuseppina De Feudis[1,#], Lorenza Garribba[1,#], Valentino Martis[1], Martina Galli[2], Marie Dumont[3], Yonatan Eliezer[4], René Wardenaar[5], Marica Rosaria Ippolito[1], Divya R Iyer[6], Andréa E Tijhuis[5], Diana CJ Spierings[5], Michael Schubert[5], Nick Rhind[6], Floris Foijer[5], Uri Ben-David[4], Daniele Fachinetti[3], Ylli Doksani[2] and Stefano Santaguida[1,7,8,*]

1. Department of Experimental Oncology at IEO, European Institute of Oncology IRCCS, Via Adamello 16, 20139 Milan, Italy

2. IFOM ETS, the AIRC Institute of Molecular Oncology, via Adamello 16, 20139, Milan, Italy

3. Institut Curie, PSL Research University, CNRS, UMR144, Paris, France

4. Department of Human Molecular Genetics and Biochemistry, Faculty of Medicine, Tel Aviv University, Tel Aviv, Israel

5. European Research Institute for the Biology of Ageing, University of Groningen, University Medical Center Groningen, 9713 AV, Groningen, the Netherlands

6. Department of Biochemistry and Molecular Biotechnology, University of Massachusetts Chan Medical School, 364 Plantation Street, Worcester, MA 01605, USA

7. Department of Oncology and Hemato-Oncology, University of Milan, Via Santa Sofia 9/1, 20122 Milan, Italy

8. Lead Contact

#These authors contributed equally

*Correspondence: stefano.santaguida@ieo.it (SS)

Keywords: aneuploidy, cancer, genome instability, MiDAS, asymmetric DNA damage segregation, senescence, mitotic errors, chromosomal instability

Abstract

Genome instability is a hallmark of cancer. The most common form of genome instability is chromosomal instability (CIN), a condition in which cells mis-segregate their chromosomes during cell division. CIN leads to aneuploidy, a state of karyotype imbalance, often found in tumors. Although the causal relationship between CIN and aneuploidy is well established, evidence is limited for a direct involvement of aneuploidy in promoting CIN. Here, we show that aneuploid cells experience DNA replication stress in their first S-phase and precipitate in a state of continuous CIN, eventually accumulating complex karyotypes. Mechanistically, we find that aneuploid cells fire dormant replication origins through a Dbf4-dependent kinase (DDK)-driven mechanism and complete replication of genomic loci through mitotic DNA synthesis (MiDAS). By following the fate of aneuploid cells, we also show that, when they divide, DNA damage can be distributed asymmetrically between daughter cells, and this may partially explain why some aneuploid cells are able to continue proliferating and others stop dividing. We further found that cycling aneuploid cells display lower karyotype complexity compared to arrested ones and increased expression of gene signatures associated to DNA repair. Interestingly, by stratifying aneuploid human cancer cells by their doubling times, we found the same DNA repair signatures to be upregulated in highly-proliferative cancer cells, which might enable them to keep proliferating despite the disadvantage conferred by aneuploidy-induced genome instability. In summary, our study reveals the origins of genome instability following induction of aneuploidy and indicates the aneuploid state of cancer cells as a point mutation-independent source of genome instability, providing an explanation for the high occurrence of aneuploidy in tumors.

Introduction

Chromosomal instability (CIN), a condition of continuous chromosome mis-segregation, is a pervasive feature of tumors [1–4]. CIN confers enhanced evolutionary capabilities on cancer cells by increasing intratumor heterogeneity and by enabling chemoresistance [5–8]. CIN leads invariably to aneuploidy, a state of karyotype imbalances, found in more than 90% of solid tumors and about 65% of blood cancers [9]. The presence of aneuploid karyotypes leads to several detrimental defects, including proteotoxic stress [10–12], metabolic alterations [13] and induction of DNA damage [10,14–18]. Importantly, the presence of aneuploid karyotypes strongly correlates with poor patient prognosis [3]. This might be due to the fact that specific aneuploid karyotypes could confer a proliferative advantage, thus fueling tumorigenesis [7,8] and promoting survival under sub-optimal conditions [5,6]. Such an advantage could be explained by the possibility that aneuploidy induces CIN (and, more broadly, genome instability), which might enable a continuous sculpting of the genome, eventually

leading to cumulative haploinsufficiency and triplosensitivity [19,20] of genes crucial for sustained proliferation. In agreement with this idea, studies in yeast have demonstrated that gain of a single chromosome leads to defective DNA damage repair [15]. Further, aneuploid strains often divide in presence of unrepaired DNA, which triggers chromosomal translocations [21]. Similar observations were made in higher eukaryotes [22]. For example, a comparison between trisomic and diploid human cells has revealed that aneuploid cells are characterized by increased frequency of lagging chromosomes in anaphase [23,24]. Thus, this evidence points at aneuploidy as an instigator of genome instability [20]. It is plausible that this instability is due to the strong impact of karyotype abnormalities on gene expression and protein homeostasis. In fact, aneuploid cells were found to display imbalances in factors critical for DNA replication (such as MCM2-7), DNA repair and mitosis [17], processes that are all fundamental for the maintenance of genome integrity. In line with this possibility, our previous studies have revealed that aneuploid cells exhibit an increased S-phase duration, display reduced DNA replication fork rate and increased fork stalling [17,18]. Due to the intrinsic genomic instability and other stresses typically associated with aneuploidy, cells with abnormal karyotypes often exhibit delayed cell cycle progression. In some cases, they even lose their proliferative capacity and stop dividing [1,18,25], resulting in their reduced sensitivity to chemotherapies [26–28].

Given the high prevalence of unbalanced karyotypes in tumors and its impact on the proliferation of cancer cells [5–8], elucidating the contribution of aneuploidy to genome instability, deciphering the molecular mechanisms by which it occurs and deconvolving its cellular consequences remain of paramount importance in cancer biology.

Here, by inducing controlled chromosome mis-segregation in otherwise pseudo-diploid human cells, we set out to identify the origins of genome instability in aneuploid cells and to understand whether protective mechanisms operate to preserve genome integrity. Our data indicate that in the first S phase following chromosome mis-segregation, aneuploid cells fire dormant replication origins through a DDK-dependent mechanism and complete replication of genomic loci through mitotic DNA synthesis (MiDAS). Importantly, those pathways, acting both in interphase and mitosis, are crucial for aneuploid cells to protect them against further genome instability. We also show that the DNA damage associated with aneuploidy can be distributed asymmetrically between daughter cells during cell division and this, at least partially, can explain why some cells (*i.e.* those who have inherited most of the damage) stop dividing. By establishing a novel method for the separation of arrested and cycling aneuploid cells, we found that cycling aneuploid cells exhibit increased expression of DNA repair genes. Interestingly, the same transcriptional signature was upregulated in cancer cells characterized by high proliferative capacity. We speculate that elevated expression of DNA damage repair genes in highly proliferative cancers is able to help them counteracting the burden associated

with genome instability, allowing them to benefit from a continuous reshuffling of the karyotype, which is crucial to sustain enhanced proliferation [5,6]. Finally, we speculate that interfering with those pathways, including DDK-mediated origin firing and MiDAS, is crucial for limiting DNA damage and might provide novel therapeutic interventions in cancer therapy. An example of this is given by ongoing clinical trials involving agents inhibiting DDK-mediated origin firing (*e.g.*, ClinicalTrials.gov Identifier: NCT03096054 and NCT05028218), and our work might help in the stratification of patients who could benefit from those treatments based on their proliferative capacity.

Results

Identification of mechanisms responsible for tolerance to aneuploidy-induced replication stress

Aneuploidy is associated with increasing genome instability [20], affecting the fidelity of both genome replication and segregation. To dissect the mechanisms through which aneuploid cells seek to limit this instability and thus keep proliferating, we quantified the direct effects of aneuploidy on genome integrity. For this, we analyzed chromosome aberrations immediately after the induction of mitotic errors (1st mitosis) and after one cell cycle later (2nd mitosis). To this aim, we synchronized untransformed and genomically-stable, pseudo-diploid hTERT RPE-1 cells at the G1/S border and, after release into the cell cycle, pulsed them with DMSO (vehicle control) or reversine, an Mps1 inhibitor widely-used to generate aneuploid cells as a consequence of chromosome segregation errors [29]. Cells were then either harvested for karyotype analysis of the 1st mitosis or, after reversine wash-out, allowed to continue in the cell cycle, and then harvested for the same purpose in the 2nd mitosis (Fig. 1a). By doing so, analysis of 1st mitosis provided a measurement of the degree of chromosome aberrations directly caused by aneuploidy induction, whereas quantification of 2nd mitosis allowed for the estimation of genome alteration as a consequence of harboring aneuploid karyotypes. By using multi-color FISH (mFISH), we found abnormal events – including gains, losses and translocations – in both the 1st and 2nd mitoses (Fig. 1b,c and Extended Data Fig. 1a,b). Importantly, the percentage of cells harboring more than 10 abnormal events more than doubled from the 1st to the 2nd mitosis (Fig. 1b,c), indicating that the aneuploid state *per se* negatively impacts genome stability. To decipher how aneuploidy affects genome integrity, we examined at high resolution the 1st S phase of newly-generated aneuploid cells. For this, we used three complementary approaches: 1) ultra-structural visualization of replication forks through electron microscopy (EM), 2) single-cell analysis of replication stress and DNA damage markers by immunofluorescence and 3) assessment of replication dynamics by DNA combing (Fig. 1d). These efforts led to three key observations. First, EM analysis of replication intermediates revealed an increase in reversed replication forks in aneuploid cells, compared to pseudo-diploid counterparts (Fig. 1e,f). Accumulation of these intermediates is

131 associated with an increased frequency of replication fork stalling [30] and is consistent with previous
132 observations of ongoing replication stress in aneuploid cells [18]. Further, aneuploid cells displayed
133 increased levels of DNA replication stress and DNA damage markers such as FANCD2 (mean foci
134 in control: 15,2 ± 1,9; aneuploid: 47,7 ± 4,6), RPA (mean foci in control: 10,6 ± 1,8; aneuploid 16,3
135 ± 2) and pChk1 (mean foci in control: 23 ± 1,8; aneuploid 33,3 ± 3,1) (Fig. 1g-l). Among them, the
136 number of FANCD2 foci per S phase cell was found to be even higher in aneuploid cells than in cells
137 treated with the DNA replication inhibitor aphidicolin, used as a positive control (FANCD2 mean
138 foci in aphidicolin-treated cells: 40,7 ± 3; RPA mean foci 49 ± 3,9; pChk1 mean foci 44,1 ± 2,6) (Fig.
139 1h). Finally, we found that fork density and origin firing rate in aneuploid cells were higher than
140 euploid counterparts (Fig. 1m-o), suggesting that dormant replication origins were fired in the 1st S
141 phase following chromosome mis-segregation events. In our previous study we reported that
142 aneuploid cells have reduced fork rate and a higher number of stalled forks as compared to euploid
143 cells (Santaguida et al., 2017). Cells activate dormant origins in response to reduced fork rate and
144 stalled forks to ensure that the genome gets fully replicated in time. Hence, we estimated origin firing
145 rate and fork density, calculated as the total number of forks per Mb of DNA [31]. The total origin firing
146 rate was 2-fold higher in aneuploid cells compared to euploid cells ($p=1,5x10^{-34}$). Consistent with the
147 origin firing data, fork density was also 1,7-fold higher in aneuploid cells ($p=7,46x10^{-13}$). Analog-
148 specific estimations for both the parameters also showed similar trends. Our data is also consistent
149 with increased origin firing observed in aneuploid human pluripotent stem cells [32]. Overall our data
150 shows that aneuploid cells struggle to complete replication and therefore activate backup mechanisms
151 such as dormant origin firing to ensure genome duplication and tolerance of replication stress.
152 Altogether, these data provide crucial insights into the effects of aneuploidy on genome integrity. We
153 find that 1) cells harboring aneuploid karyotypes tend to accumulate increasing levels of chromosome
154 abnormalities. Importantly, 2) those defects might be the consequence of DNA replication stress, and
155 3) are correlated with a higher incidence of replication fork reversal and increased DNA damage
156 markers. Finally, 4) at the same time, aneuploid cells also show an increased usage of dormant origins,
157 which we speculate it might act as a mechanism to tolerate aneuploidy-induced replication stress.
158
159 **Aneuploid cells rely on DDK to cope with replication stress**
160 Dormant origin firing is a well-known rescue mechanism that protects cells during replication stress
161 [33]. To test whether aneuploid cells would also rely on this salvage mechanism, we inhibited the
162 activity of DDK, a key player in origin firing [34–37]. For this, aneuploid cells or pseudo-diploid
163 counterparts (generated as in Fig. 1a) were arrested in late G1 (after the 1st mitosis) and then released
164 in the presence or absence of the DDK inhibitor XL413 [38] (Fig. 2a). After 6 hours, cells were pulsed

165 with the thymidine analogue ethynyl deoxy-uridine (EdU) for 30 minutes to label S phase cells and
166 then fixed and stained for FANCD2, RPA and pChk1. We find that inhibition of DDK led to
167 significantly increased levels of FANCD2 (mean foci in control: 40,9 ± 2,9; control + DDKi: 52,6 ±
168 2,9; aneuploid 72,2 ± 3,5; aneuploid + DDKi: 84,5 ± 4,9), RPA (mean foci in control: 56,3 ± 3,7;
169 control + DDKi: 36,2 ± 2,9; aneuploid 83,5 ± 5,8; aneuploid + DDKi: 103,9 ± 6,4) and pChk1 (mean
170 foci in control: 44,1 ± 2,6; control + DDKi: 44,9 ± 2,8; aneuploid 62,9 ± 4,2; aneuploid + DDKi: 74,7
171 ± 4,2) in aneuploid cells, indicating that replication stress is exacerbated when interfering with
172 dormant origin firing through DDK inhibition (Fig. 2b-g). These results prompted us to test whether
173 DDK activity, and its involvement in dormant origin firing, would also be critical for aneuploid cell
174 proliferation. Interestingly, we found that aneuploid cells were more sensitive to DDK inhibition
175 compared to pseudo-diploid counterparts (Fig. 2h,i), indicating that they rely more than euploid cells
176 on the function of DDK to survive. Altogether, our data show that DDK-mediated origin firing
177 represents a protective mechanism that acts in S phase of aneuploid cells to limit replication stress.
178 Importantly, inhibition of this mechanism exacerbates replication stress in aneuploid cells and
179 reduces their viability.
180

181 **Aneuploid cells undergo mitotic DNA synthesis to limit the consequences of replication stress**
182 **on genome stability**

183 DNA replication stress - defined as any slowing or stalling of replication fork progression and/or
184 DNA synthesis [39] - impacts mitotic fidelity [40–42]. Thus, we thought to study how the events occurring
185 in the 1st S phase of aneuploid cells affect the following cell division. To this aim, we performed live-
186 cell imaging experiments with hTERT RPE-1 cells stably expressing PCNA-GFP and H2b-RFP. This
187 allowed to monitor S phase length through the measurement of time elapsed between appearance and
188 disappearance of PCNA foci (a well-known feature of this DNA clamping factor, [43]) and mitotic
189 timing and quality by tracking chromosomes through H2b. Cells were synchronized with thymidine,
190 then pulsed with reversine while they were transiting through the 1st mitosis. Cells were then washed-
191 out and imaged every 10 minutes for 72 hours in order to evaluate the duration of the first S phase
192 after chromosome mis-segregation and the quality of the 2nd mitosis (Fig. 3a,b). First, we found that
193 aneuploid cells displayed a longer S phase compared to euploid controls (mean S phase length in
194 control: 540,1 ± 17,82; aneuploid: 662,5 ± 29,89. Extended Data Fig. 1c), in agreement with the fact
195 that they experience ongoing DNA replication stress and in line with previous reports [17,18]. Next, we
196 decided to correlate S phase length to the quality of the 2nd mitosis. Thus, we classified mitotic figures
197 in "normal mitoses", for those not displaying defects, and "abnormal mitoses", for those showing
198 mitotic errors, including chromatin bridges, lagging chromosomes or micronuclei in the following

199 G1. Interestingly, we found a positive correlation between S phase length and frequency of abnormal
200 mitoses (mean S phase length in control: 603,3 ± 55,4; aneuploid: 728,7 ± 46,2) (Fig. 3c). Further,
201 aneuploid cells that displayed mitotic errors spent more time in mitosis (Fig. 3d), which we could
202 fully attribute to spindle-assembly checkpoint activation, since SAC inhibition rescued this delay
203 (Extended Data Fig. 1d).
204 Based on the evidence that aneuploid cells suffer from replication stress in the 1st S phase following
205 chromosome mis-segregation events, we wanted to investigate whether they would attempt to finish
206 DNA replication in the subsequent mitosis, as previously discovered in cancer cells as a consequence
207 of S phase stress [44]. In order to evaluate mitotic DNA synthesis (MiDAS) pathway activation,
208 aneuploid cells generated as in Fig. 1a were arrested at the G2/M boundary with the CDK1 inhibitor
209 RO3306 and released in the presence of EdU and Colcemid to monitor sites of active DNA synthesis
210 in prometaphase cells. We observed that the number of EdU foci per spread was significantly higher
211 in aneuploid cells in comparison to the control (mean EdU foci in control: 0,1 ± 0,04; aneuploid: 0,9
212 ± 0,1; Fig. 3e,f). The DNA replication inhibitor aphidicolin was added in S phase as replication stress
213 inducer (mean EdU foci: 2,6 ± 0,3) [45]. Next, to test the efficacy of MiDAS in fixing unfinished DNA
214 replication, we inhibited the pathway and evaluated the consequences on genome stability in the
215 following G1 (Fig. 3g). To this aim, we first tested if MiDAS could be inhibited by adding a high
216 dose of aphidicolin in mitosis similarly as observed in cancer cells [44,46,47]. Our results showed that
217 indeed this was the case, since the number of EdU foci per prometaphase cell was significantly
218 reduced upon addition of aphidicolin in mitosis (mean EdU foci in control: 0,2 ± 0,1; control +
219 MiDASi: 0,1 ± 0,03; aneuploid: 1,3 ± 0,2; aneuploid + MiDASi: 0,5 ± 0,1; Fig. 3H and I). As readouts
220 of genome instability, we analyzed 53BP1 bodies and micronuclei in the G1 phase after the 2nd mitosis
221 in which MiDAS had occurred. We found that both 53BP1 bodies per cell and the frequency of G1
222 cells with micronuclei were significantly increased in aneuploid cells in which MiDAS was inhibited
223 in comparison with those in which MiDAS occurred properly (Fig. 3j-l). This correlation was also
224 observed in aphidicolin-treated cells (mean EdU foci: 4,5 ± 0,6; + MiDASi: 0,7 ± 0,3), in agreement
225 with previous studies [44]. Altogether, our data demonstrate that MiDAS acts as a safeguard mechanism
226 in the 2nd mitosis to prevent genome instability from further increasing.
227
228 **Dormant origin firing and MiDAS protect aneuploid cells from further increase in genome**
229 **instability**
230 The results obtained from the characterization of the first S phase after chromosome mis-segregation
231 and the subsequent mitosis revealed two protective mechanisms operating in aneuploid cells with the
232 role of limiting genome instability. To test if the combined action of these two pathways indeed serves

233 to protect aneuploid cells, we simultaneously inhibited DDK in S phase and MiDAS in the subsequent
234 M phase and evaluated DNA damage and chromosomal aberrations in the following G1 phase (Fig.
235 4a). As DNA damage markers, we used FANCD2, a reliable replication stress/DNA damage marker
236 in aneuploid cells (Fig. 1h), and γH2AX, an early marker of DNA double-stranded breaks [48]. To
237 specifically look at G1 cells, we used cytochalasin B to block cytokinesis and analyze daughter cells
238 (Fenech and Morley 1985). We observed that the number of both FANCD2 and γH2AX foci was
239 significantly higher in aneuploid cells in which DDK and MiDAS were inhibited compared to
240 aneuploid cells in which only either DDK or MiDAS was hindered (Fig. 4b-d). Interestingly,
241 inhibition of those pathways led to an increase in FANCD2 and γH2AX foci also in euploid cells,
242 highlighting that their proper functioning is crucial for maintaining genome integrity. Then, to assess
243 the frequency of chromosomal aberrations upon DDK and MiDAS inhibition, G1 cells were treated
244 with the PP1/PP2A phosphatase inhibitor calyculin A to induce premature DNA condensation [50] and
245 obtain metaphase-like spreads. By mFISH analysis, we were able to observe an almost 2-fold increase
246 in the percentage of cells with translocations between aneuploid cells in which DDK and MiDAS
247 were or were not inhibited (mean percentage of cells with at least 1 translocation in aneuploid cells:
248 33,4; in aneuploid cells + DDKi + MiDASi: 63,2) (Fig. 4e-g). Taken together, these data indicate that
249 the presence of both pathways protects aneuploid cells from further increasing their genome
250 instability.
251 Interestingly, while scoring DNA damage in G1 cells we noticed that distribution of FANCD2 or
252 γH2AX foci in aneuploid cells was not always symmetric between daughter cells. Thus, we decided
253 to specifically look at the pattern of DNA damage inheritance in the aneuploid sample and the euploid
254 control, along with aphidicolin-treated cells where it has been recently shown that DNA damage can
255 be distributed asymmetrically between daughters [51]. Our data indicated that FANCD2 and γH2AX
256 foci were asymmetrically distributed in about 20% and 10% of aneuploid daughter cells, respectively
257 (Fig. 4h-j). These data suggested that non-random distribution of DNA damage between aneuploid
258 daughter cells could underlie the difference in proliferation observed among aneuploid cells [18,25].
259
260 **A novel method to separate arrested and cycling aneuploid cells**
261 The asymmetric inheritance of DNA damage and cell fate determinants have been hypothesized to
262 underlie stem cell self-renewal [52,53]. Thus, based on asymmetric portioning of DNA damage markers
263 in aneuploid cells (Fig. 4h-j), we reasoned that, like stem cells, they might segregate DNA damage
264 asymmetrically, partially explaining why some aneuploid cells can keep cycling while others get
265 arrested and enter senescence [18,25]. To test this hypothesis, we first needed to confirm that a proportion
266 of aneuploid cells indeed gets arrested in the cell cycle and becomes senescent over time. Hence, we

267 let aneuploid cells progress for about 3 cell cycles before harvesting them for β-galactosidase staining,
268 a widely used marker of senescence [54]. As a positive control, we used cells treated with doxorubicin
269 for 7 days, as DNA damage is an established senescence-inducer [55]. Our results indicated that, as
270 expected [18], there was a sub-population of senescent cells in the aneuploid sample (Fig. 5a). In order
271 to characterize, in detail, the aneuploid cells that were still able to cycle and those that underwent
272 senescence, we decided to establish a novel method for their isolation and separation. For this, we
273 reasoned that the main (and, at the same time, potentially exploitable) difference between aneuploid
274 cycling and arrested cells is that the latter are senescent. Thus, we developed a FACS-sorting based
275 assay employing the fluorescent substrate of the β-galactosidase enzyme (which is highly active in
276 senescent cells) 9H-(1,3-dichloro-9,9-dimethylacridin-2-one-7-yl) β-d-galactopyranoside (DDAOG)
277 [56]. We then exposed aneuploid cells to DDAOG and separated cells that were able to metabolize it
278 (*i.e.*, senescent cells) from those that could not metabolize it (*i.e.*, cycling cells) (Fig. 5b,c; Extended
279 Data Fig. 2a). First, we confirmed that sorted cells were indeed either arrested or cycling by β-
280 galactosidase staining and found the former to be highly reactive to senescence-associated β-
281 galactosidase staining (Fig. 5d). Further, we used hTERT FUCCI RPE-1 cells [57] to obtain the cell
282 cycle profile of the two sorted aneuploid cell populations, together with the aneuploid sample before
283 sorting and the euploid control (Extended Data Fig. 2b). Our data confirmed that aneuploid cells
284 positive for DDAOG were indeed arrested, since the vast majority of them (86 ± 14,1%) were stuck
285 in G1, as expected for senescent cells. On the other hand, negative ones were able to proliferate
286 (Extended Data Fig. 2c and Fig. 5e,f) and the percentage of G1 cells were 24% (± 8,5%) (Extended
287 Data Fig. 2c and Fig. 5e,f). Collectively, these data indicate that our method allows for the successful
288 separation and recovery of arrested and cycling aneuploid cells that could be used for further analysis
289 and characterization of the two populations.
290
291 **Cell cycle arrest in aneuploid cells is due to both DNA damage and karyotype complexity**
292 To validate our hypothesis that asymmetric inheritance of DNA damage would contribute to cell
293 cycle arrest in aneuploid cells, we evaluated DNA damage in cycling and arrested aneuploid cells,
294 together with aneuploid cells before sorting and the euploid control. Our data indicate that aneuploid
295 arrested cells display increased levels of FANCD2 and γH2AX foci compared to aneuploid cycling
296 cells (mean FANCD2 foci in aneuploid arrested: 71,8 ± 3,9; in aneuploid cycling: 46,9 ± 2,2; mean
297 γH2AX foci in aneuploid arrested: 6,4 ± 1,1; in aneuploid cycling 2,4 ± 0,5) (Fig. 5g-i). Further, we
298 also analyzed the karyotype of cycling and arrested aneuploid cells by single-cell whole genome
299 sequencing (scWGS) and observed an increased frequency of cells with at least 3 aneuploid

300 chromosomes in arrested aneuploid cells (Fig. 5j,k). Altogether, these data show that both DNA
301 damage and severe karyotype imbalances contribute to cell cycle arrest in aneuploid cells.
302
303 **Cycling aneuploid cells display increased expression of DNA repair genes**
304 In line with reduced DNA damage and karyotype abnormalities in the aneuploid cells that retained
305 their proliferation capacity, we found that the frequency of mitotic errors (such as anaphase bridges
306 and micronuclei) in aneuploid cycling cells was comparable to that of the controls for at least 3
307 generations by live-cell imaging (Fig. 6a-c). This result suggests that the karyotype of these cells is
308 likely to remain stable over time, which is indicative of low levels of genome instability in aneuploid
309 cycling cells. This also indicates that aneuploidy does not invariably leads to CIN and it suggests that
310 specific chromosome assortments are more prone than others to be genomically unstable, reflecting
311 imbalances of specific genes crucial for genome replication and segregation. Having established a
312 tool to separate the two sub-populations of aneuploid cells, we turned our attention to the
313 identification of features distinguishing aneuploid cycling cells from those that arrested. To address
314 this question, we decided to analyze their transcriptional signatures via RNAseq. This analysis
315 revealed that the two samples are indeed quite different (Fig. 6d). In particular, aneuploid arrested
316 cells displayed overexpression of p53 and inflammation-related genes, in agreement with previous
317 findings [18]. Conversely, aneuploid cycling cells, as expected based on their retained ability to divide,
318 exhibited increased expression of cell cycle genes compared to aneuploid arrested cells. Interestingly,
319 we also noticed that DNA damage and repair genes were overexpressed in aneuploid cycling cells
320 (Fig. 6d and Extended Data Table 1). To further highlight differences in gene expression between the
321 two subpopulations of aneuploid cells, we generated a heatmap showing that the main DNA repair
322 related gene categories are more expressed in cycling *vs* arrested aneuploid cells (Fig. 6e). In line
323 with this, when exposed to ionizing radiation (IR), cycling aneuploid cells were able to repair DNA
324 damage more efficiently than the arrested ones (Extended Fig. 3a and Fig. 6f,g). Indeed, we measured
325 a faster decay kinetics of γH2AX and 53BP1 levels in the cycling population compared to the arrested
326 one (Extended Fig. 3a and Fig. 6f,g). Non-sorted aneuploid cells were also included in the analysis,
327 and they turned out to have a lower efficiency compared to the euploid controls in fixing IR-induced
328 DNA damage (Extended Fig. 3). Importantly, the activation of DNA damage repair pathways in
329 aneuploid cells is consistent with our recent findings in cancer [27] and untransformed cells [58]. We
330 therefore hypothesized that higher expression of DNA damage repair genes would confer a growth
331 advantage to the cells. To confirm this, we turned to the CCLE (Cancer Cell Line Encyclopedia)
332 database [59,60] to analyze the association between doubling time and DNA damage repair gene
333 expression in more than 400 human cancer cell lines. We divided the cell lines into top and bottom

334 quartiles based on their doubling times, and then compared their gene expression profiles. Cells with
335 a low doubling time (<35 hours) exhibited increased expression of DNA repair related gene signatures
336 in comparison to cells with a high doubling time (>65 hours) (Fig. 6i-j), suggesting that elevated
337 expression of this gene category can confer a proliferative advantage to aneuploid cells and make
338 them able to cycle despite the disadvantage conferred by the aneuploid status. Altogether, our data
339 revealed the existence of protective mechanisms in aneuploid cells, namely DDK-mediated origin
340 firing in S phase and MiDAS in the subsequent mitosis, which operate in order to limit their genome
341 instability (Fig. 7). Also, cell cycle arrest in aneuploid cells is due to not only the degree of karyotype
342 aberrations but also to the levels of DNA damage harbored by the cells. Importantly, an increased
343 capacity to repair DNA damage confers a proliferative advantage not only to untransformed but also
344 to cancer aneuploid cells (Fig. 7).
345

346 **Discussion**

347 Genome instability is an established hallmark of cancer [61]. Its most common form is chromosomal
348 instability (CIN), which has been shown to promote tumorigenesis and confer proliferative
349 advantages to cancer cells [5–8]. Because CIN refers to a condition of continuous chromosome
350 missegregation, this indicates that genomic instability can directly cause aneuploidy. In this study,
351 we demonstrated that aneuploidy can also instigate genome instability. By combining biochemical
352 and live cell imaging experiments with single-molecule replication-mapping technologies and single-
353 cell multi-omics analysis, we found that the acquisition of unbalanced karyotypes can directly
354 contribute to genome instability, which in turn yields a diverse array of karyotypic landscapes. This
355 effect feeds a self-sustaining loop, in which aneuploidy leads to CIN, thus generating more aneuploid
356 daughter cells able to propagate genome diversity through continuous errors during genome
357 replication and segregation.
358 Previous reports have shown that aneuploid cells can experience replication stress [17,18]. Here, we
359 show that dormant origin firing operates during the first S phase following chromosome mis-
360 segregation and acts as a protective mechanism to cope with replication stress. The fact that DDK
361 inhibition impacts on aneuploid cell viability reveals the importance of this pathway in the context of
362 karyotype imbalances. Although we identified DDK-mediated dormant origin firing as a protective
363 mechanism operating in the 1st S phase of aneuploid cells, it is still unclear what exactly triggers it,
364 *i.e.* what are the actual sources of replication stress in cells with abnormal karyotypes. Many possible
365 sources of DNA replication stress have been described so far, which include difficulties in the
366 template DNA (*e.g.*, repetitive sequences and/or secondary structures), collisions between the
367 replication fork and the transcriptional machinery, nucleotide pool imbalances and scarcity of

368 replication factors to perform DNA synthesis [39]. Among them, insufficient amount of replication
369 factors seems to be the most likely cause of replication stress in aneuploid cells, based on the fact that
370 decreased levels of MCM2-7 proteins were reported in RPE-1 and HCT116 stable aneuploid clones
371 with defined trisomies [17]. Also, a recent work has revealed that tetraploid cells encounter replication
372 stress as a result of insufficiency of DNA replication factors [62], a mechanism that could also apply to
373 aneuploid cells. Because in our system we observe dormant origin firing, we speculate that the
374 limiting DNA replication factors are those downstream of origin firing, such as PCNA, RFC and
375 DNA polymerases [63]. Future studies will be aimed at exploring this possibility, with the goal of
376 elucidating the contributions of those factors in DNA replication of aneuploid cells. This line of study
377 might also open novel therapeutic interventions through selective targeting of aneuploid cancer cells
378 by targeting those limiting DNA replication factors.
379 Along this line, another important implication of our finding that DDK and MiDAS play a central
380 role in helping cells coping with aneuploidy is that these mechanisms could well be targetable
381 vulnerabilities of aneuploid cancers. Although it might be challenging to selectively target MiDAS -
382 its key players SLX4-MUS81, RAD52 and POLD3 [44,46] are also involved in other processes beyond
383 MiDAS, such as homologous recombination (HR) repair and canonical S phase DNA replication –
384 things could be different for DDK. In particular, the DDK inhibitor TAK-931 was recently tested in
385 a phase 2 clinical trial for the treatment of advanced solid tumors [64]. Based on our study, we speculate
386 that this drug (and similar ones) could be combined with inhibitors of DNA repair, such as the
387 products of genes playing a role in HR repair, since they were the most differentially regulated in our
388 analysis (Extended Table 1). Thus, the combined inhibition of DDK and HR repair factors could
389 potentially be very effective to treat aneuploid cancers. This approach would have the great advantage
390 of being highly selective against cancer aneuploid cells, lowering the side-effects of the DNA repair-
391 based cancer therapies and the frequent chemoresistance associated with them [65].
392 In summary, by providing a detailed characterization of the role of aneuploid karyotypes in the
393 acquisition of aggressive cancer-like features, we demonstrate that aneuploidy provides a point
394 mutation-independent source of genome instability. Although this might offer a source of karyotypic
395 variations capable of enabling proliferative capacity of cancer cells, it also leads to extensive DNA
396 damage. Thus, we speculate that aneuploidy-induced genome instability might be a double-edged
397 sword for cancer cells. On one hand, it is crucial for providing genome plasticity, on the other it might
398 be extremely deleterious because of continuous DNA damage and replication stress. We propose that
399 cancer cells solve this issue by limiting DNA damage - through upregulation of DNA repair genes -
400 to a level compatible with cell proliferation. At the same time, this allows them to keep some degree
401 of genomic instability and thus to continuously sample diverse karyotypic landscapes. Our

402 observation shed new light on the bidirectional association between aneuploidy and genomic
403 instability and propose new approaches for the selective eradication of aneuploid tumors.
404

405 # Methods

406 **Cell culture conditions**

407 hTERT RPE-1 cells, including those expressing H2b-RFP and PCNA-GFP or H2b-GFP or LCK-
408 GFP (all generated in house) and the hTERT Fluorescent Ubiquitination-based Cell Cycle Indicator
409 (FUCCI) RPE-1 (kind gift of Professor Simona Polo, IFOM, Milan, Italy), were all tested free of
410 mycoplasma contamination using Myco Alert (Lonza) according to manufacturer's instructions. All
411 the cells were maintained in a humified environment at 37 degrees with 5% CO_2 and cultured in
412 Dulbecco's modified Eagle's medium (DMEM) supplemented with 10% fetal bovine serum and 1%
413 penicillin/streptamycin.
414

415 **Cell synchronization and treatments**

416 To harvest metaphase cells for mFISH analysis, hTERT RPE-1 cells were pulsed with the Mps1
417 inhibitor reversine (500nM, Cayman Chemical) or the vehicle control (dimethyl sulfoxide, DMSO)
418 for 24 hours and then harvested for karyotype analysis either immediately after the pulse ('1st
419 mitosis') or 24 hours later ('2nd mitosis'). In both cases, colcemid (100ng/ml, Merck Millipore) was
420 added 2 hours before harvesting the cells in order to block cells in prometaphase. To perform ultra-
421 structural analysis of replication intermediates and analyze replication dynamics, cells were treated
422 as above and analyzed immediately after the 24-hour reversine/DMSO pulse.
423 To analyze DNA replication stress markers in S phase, hTERT RPE-1 cells were plated onto
424 fibronectin (5µg/ml, Sigma-Aldrich) coated coverslips at approximately 30% confluence and
425 synchronized at the G1/S boundary with thymidine (5mM, Merck Millipore) for 24 hours. After 3
426 washes in 1X PBS, cells were pulsed for 18 hours with reversine or vehicle control (DMSO) and
427 released in the presence of mimosine (0,5mM, Merck Millipore) for 18 hours. After 3 washes in 1X
428 PBS, cells were incubated for 6 hours in the presence or absence of aphidicolin (400nM, Merck
429 Millipore) or the DDK inhibitor XL413 (10µM, Aurogene) prior to fixation for immunofluorescence.
430 The thymidine analog ethynyl deoxy-uridine (EdU) was added at a final concentration of 10µM
431 during the last 30 minutes to label S phase cells.
432 To assess S phase length and quality of the subsequent mitosis by time-lapse microscopy, after plating
433 onto a fibronectin-coated glass 12wellplate, hTERT RPE-1 cells were blocked in G1/S with
434 thymidine for 24 hours, then washed out, pulsed with reversine/DMSO for 18 hours and filmed for
435 72 hours.

436 For MiDAS detection, hTERT RPE-1 cells were treated as above and, after reversine/DMSO
437 washout, released in RO3306 (7,5μM, Merck Millipore) for 12 hours to arrest them in late G2 phase.
438 Then, after 3 washes in 1X PBS, cells were released in mitosis in the presence of EdU 20μM and
439 colcemid for 2 hours to harvest prometaphase cells for MiDAS detection. Aphidicolin 400nM was
440 added to a subpopulation of cells pulsed with DMSO just after DMSO washout in order to induce
441 DNA replication stress (positive control). To investigate the consequences of MiDAS inhibition in
442 G1 cells, cells were plated and treated as above. After RO3306 washout, cells were released in EdU
443 20μM in the presence or absence of aphidicolin (2μM, Merck Millipore) for 40 minutes (for
444 prometaphase cells) or 3 hours (for G1 cells) prior to fixation of immunofluorescence.
445 In order to harvest daughter pseudo-G1 cells, after thymidine and reversine pulses, hTERT RPE-1
446 LCK-GFP cells were released in the presence or absence of XL413 10μM and arrested in late G2
447 phase with RO3306 7,5μM. After drug washout, cells were incubated in the presence or absence of
448 aphidicolin 2μM for 3 hours together with cytochalasin B (3μg/ml, Merck Millipore) to block
449 cytokinesis prior to fixation for immunofluorescence.
450 To obtain metaphase-like spreads from G1 cells, calyculin A (50ng/ml, Sigma-Aldrich) was added
451 for 45 minutes to G1 cells treated as above to induce premature chromosome condensation, prior to
452 harvest for mFISH analysis.
453 To evaluate β-galactosidase positivity in aneuploid cells, after reversine washout, hTERT RPE-1 cells
454 were allowed to progress for about 60 hours before fixation. The same protocol was used to generate
455 aneuploid cells for sorting, including hTERT FUCCI RPE-1 and hTERT RPE-1 H2b-GFP cells. After
456 sorting, some cells were replated and fixed 16 hours later to perform β-galactosidase staining, while
457 some other were replated for live cell imaging experiments or directly harvested as frozen pellets for
458 RNA extraction. As a positive control for senescence, cells continuously treated with doxorubicin
459 (200nM, Merck Millipore) for 7 days were used.
460
461 **Multicolor fluorescence in situ hybridization (mFISH)**
462 After the treatments described above, hTERT RPE-1 cells blocked in prometaphase or G1 cells in
463 which premature condensation was induced were trypsinized and centrifuged to obtain cell pellets.
464 Cell pellets were resuspended in KCl 75mM and incubated for 10 min in a 37 degrees waterbath.
465 After centrifugation, cells were fixed in freshly-prepared Carnoy solution (methanol-acetic acid in a
466 3:1 ratio) while vortexing and then incubated for 30 minutes at room temperature (RT). After a wash
467 in freshly-prepared Carnoy solution, minimum volume of fixative was left to resuspend the pellet and
468 cells were dropped onto glass slides. mFISH staining was performed following manufacturer's
469 instructions (MetaSystems). The Metafer imaging platform (MetaSystems) and the Isis software

470 (MetaSystems, version 5.5) were used for automated acquisition of the chromosome spread and
471 mFISH image analysis.
472
473 **Ultra-structural analysis of replication intermediates**
474 For EM analysis, hTERT RPE-1 cells were pulsed for 24 hours with reversine or vehicle control
475 (DMSO) and then harvested. Immediately after, cells were psoralen-crosslinked *in vivo* to stabilize
476 replication intermediates as described in [66]. The cell suspension was first incubated with 30 µg/ml 4,
477 5′, 8-trimethylpsoralen (2mg/ml, Sigma) for 5 min in the dark and then exposed to 365 nm UV light
478 for 8 min in a UV Stratalinker 1800, (Stratagene), with 365 nm UV bulbs (model UVL-56, UVP) at
479 2–3 cm from the light source. The incubation and irradiation steps were repeated three more times (4
480 cycles total). Genomic DNA (gDNA) was extracted with phenol-chloroform as described in [66]. 50 µg
481 of gDNA were digested with KpnI and passed through a QIAGEN Genomic-tip 20/G column
482 (QIAGEN) to enrich for replication intermediates, as described by Zellweger and Lopes [67]. EM
483 spreads and imaging was performed as described in [68].
484
485 **Immunofluorescence analysis and EdU detection**
486 At the end of the treatments described above, hTERT RPE-1 or hTERT RPE-1 LCK-GFP cells were
487 washed once in 1X PBS and then fixed in 4% paraformaldehyde (PFA) for 15 minutes at RT. After
488 3 washes in 1X PBS, cells were blocked in 3% bovine serum albumin (BSA) + 0.5% Triton-X in 1X
489 PBS for 30 minutes and incubated with the following primary antibodies diluted in the same buffer
490 for 90 minutes at RT: anti-FANCD2 (Novus Biologicals) 1:400, anti-RPA (Abcam) 1:200, anti-
491 pChk1 (Cell Signaling Technology) 1:200, anti-53BP1 (Abcam) 1:1000, anti-γH2AX (Millipore)
492 1:400. After 3 washes in 1X PBS, cells were incubated with secondary antibodies (ThermoFisher
493 Scientific) diluted 1:400 in 3% BSA + 0.5% Triton-X in 1X PBS for 45 minutes at RT in the dark.
494 Coverslips were then mounted on glass slides using Vectashield Antifade Mounting Medium with
495 DAPI (Vectorlabs).
496 Where indicated, immunofluorescence was combined with EdU detection. Briefly, after the blocking,
497 EdU detection was performed using the Click-iT EdU Cell Proliferation kit for Imaging
498 (ThermoFisher Scientific) following the manufacturer's instructions. After the washes, incubation of
499 the cells in primary antibodies and the subsequent steps of immunofluorescence were performed as
500 indicated above.
501
502 **DNA fiber analysis**
503 Cells were labeled sequentially with IdU (green [G]) and CldU (red [R]) and were harvested and

504 processed as described in [18]. Data was collected from 2 independent experiments. A total of 47 and
505 54 Mb of DNA and 33 and 38 Mb of DNA was collected from the control and the aneuploid cells,
506 respectively. Data analysis was performed as described in detail in [31]. Please note that the order of
507 labeling is reversed (CldU → IdU) in the experiments described in [31], therefore, the interpretation of
508 patterns is also reversed as compared to this article. Briefly, origin firing rate is the total number of
509 origins that fired during the first and the second analog in each fiber divided by the total length of
510 the un-replicated DNA in that fiber and the total length of the analog labeling pulses (120 minutes).
511 Origins that fire during the first analog will appear as Red-Green-Red [RGR] and origins that fire
512 during the second analog will appear as Red [R] events. However, origins that fire during the first
513 analog will appear as RGR only if both the forks progress into the second analog. The origins will
514 appear as RG or GR if either of the fork stalls or as G if both the forks stall. Thus, the total number
515 of origins in each fiber was estimated by accounting for the probability of forks stalling.
516 Fork density is the total number of forks in each fiber divided by the total length of the un-replicated
517 DNA of that fiber. Origins and termination events account for 2 forks each and unidirectional fork
518 events account for 1 fork each. However, some of the unidirectional forks could be an origin whose
519 left or rightward fork is stalled. Thus, the total number of forks on each fiber was estimated by
520 accounting for the probability of forks stalling. Please see [31] for calculation of fork stall rate and how
521 the probability of fork stalling was used to estimate the final origin firing rate and fork density for
522 each fiber.
523
524 **Cell proliferation assay**
525 After thymidine synchronization and reversine/DMSO pulse as above, hTERT RPE-1 cells were
526 trypsinized, counted and plated into a 96wellplate in the presence of XL413 10μM or the vehicle
527 control (DMSO). Drugs were re-added fresh every 48-72 hours during the 120 hour -treatment. Then,
528 cell viability was assessed by using the CellTiter-Glo Luminescent cell viability assay (Promega)
529 following manufacturer's instructions.
530
531 **Live cell imaging**
532 To monitor S phase length and M phase duration and quality, cells were treated as above. After
533 reversine/DMSO washout, fresh medium without phenol red was added to the cells. Cells were
534 imaged every 10 minutes for 72 hours under a 20x objective with an inverted Nikon Eclipse Ti
535 microscope equipped with incubator for live cell imaging. The same microscope and acquisition
536 settings were used to film aneuploid cycling cells after sorting for 72 hours to assess their genome
537 stability.

538

539 **MiDAS detection**

540 To detect MiDAS on metaphase spreads, after incubation in EdU and colcemid as above, cells were
541 treated similarly to those for mFISH analysis. After cell dropping onto glass slides and complete
542 evaporation of the Carnoy solution, slides washed in 1X PBS in agitation. EdU detection was
543 performed with the Click-iT EdU Cell Proliferation kit for Imaging (ThermoFisher Scientific)
544 according to manufacturer's instructions with some minor modifications as described in [69]. Slides
545 were then mounted using Vectashield Antifade Mounting Medium with DAPI.

546 To detect MiDAS on prometaphase cells, at the end of the treatments described above, cells were
547 fixed in 4% PFA for 15 minutes at RT, then washed 3 times in 1X PBS. EdU detection was performed
548 as above [69] and coverslips were then mounted on glass slides using the same mounting medium as
549 above.

550

551 **Distribution of DNA damage in pseudo-G1 cells**

552 First, the number of FANCD2 and γH2AX foci per daughter cell was counted. Based on the average
553 number of foci per cell, cells with less than 6 or 4 foci (for FANCD2 or γH2AX, respectively) were
554 excluded from the analysis. Then, the total number of foci between the two daughters (*e.g.* 13+10)
555 was calculated and divided by 2 to obtain the number of foci predicted to be inherited by each
556 daughter cell in case of symmetric distribution of DNA damage (*e.g.* 23 divided by 2 is equal to 11,5).
557 Subtraction or addition of this number to the total number of foci in the daughters was used to set a
558 threshold for asymmetric distribution of DNA damage, *e.g.* 23-11,5= 11,5, which is the lowest
559 threshold; 23+11,5= 34,5, which is the highest threshold; if a daughter cell has less than 11,5 or more
560 than 34,5 foci the distribution of DNA damage is considered as non-random (non-random
561 distribution, NDD).

562

563 **β-galactosidase staining**

564 DMSO- and reversine-pulsed cells allowed to progress for about 72 hours after DMSO/reversine
565 washout, together with sorted cycling and arrested aneuploid cells, were plated into a 6 well plate at
566 $1x10^6$ cells/well and allowed to attach overnight. Then, cells were stained using the Senescence β-
567 Galactosidase Staining Kit (Cell Signaling Technology) following manufacturer's instructions.

568

569 **Sorting of aneuploid cells**

570 Cells were plated into 150 mm plates (900.000 cells/plate) and treated as above. After
571 reversine/DMSO washout, cells were allowed to divide for about 60 hours. Then, they were incubated

572 with the fluorescent substrate of the β-galactosidase enzyme DDAO-Galactoside (DDAOG) 10mM
573 for 90 minutes. At the end of the incubation, cells were harvested for FACS sorting and acquired
574 using a FACSAria Fusion flow cytometer (BD). Cells were gated for singlets and alive cells and then
575 FSC-A, SSC-A and Alexa-647 intensity were used to distinguish cycling from arrested cells, *i.e.*
576 cycling cells were gated using the same Alexa-647 Mean Fluorescence Intensity of the control sample
577 without DDAOG, while arrested cells were gated imposing 0,1% on Alexa-647 signal to the control
578 sample without DDAOG. FlowJo was used to perform data analysis and generate the plots in Figure
579 5 and Extended Data Fig. 2.
580
581 **Cell cycle profile analysis through the FUCCI system**
582 hTERT FUCCI RPE-1 cells were used to generate euploid, aneuploid, cycling aneuploid and arrested
583 aneuploid cells as described above. After the sorting, cells were plated in a 12wellplate, allowed to
584 attach overnight and then filmed using an inverted Nikon Eclipse Ti microscope with a 40x objective
585 equipped with incubator for live cell imaging. Brightfield, green (GFP) and red (mCherry) channels
586 were used to acquire the movie. Images were taken every 30 minutes for 24 hours. Cell cycle stage
587 was determined based on nuclear color: red nuclei were scored as G1 phase, while yellow and green
588 nuclei were scored as S/G2 phase; lastly, M phase was characterized by uncolored nuclei of two
589 dividing cells [57].
590
591 **Sample processing for RNAseq**
592 Aneuploid cycling and arrested cells post sorting were centrifuged and cell pellets were obtained.
593 RNA was extracted from them using a RNeasy kit (QIAGEN) and its quality was assessed with a
594 Bioanalyzer 2100 (Agilent). Then, for each sample, total RNA was depleted of ribosomal RNA and
595 the RNAseq libraries were prepared with the Illumina TruSeq Stranded Total RNA kit following the
596 manufacturer's protocol. Briefly, after the fragmentation of RNA using divalent cations at elevated
597 temperature, cDNA was synthesized, end-repaired and 3'-end-adenylated. Following adapter
598 ligation, libraries were amplified by PCR. Amplified libraries were checked on a Bioanalyzer 2100
599 (Agilent) and quantified with picogreen reagent. Libraries with distinct TruSeq adapter UDIndexes
600 were sequenced for 50 bases in the paired-end mode with 35 million reads in coverage on a Novaseq
601 6000 sequencer.
602
603 **Data analysis for RNAseq**
604 RNA reads were aligned to the GRCh38 primary assembly with Ensembl 104 [70] gene annotations
605 using. STAR 2.7.9a [71]. Gene counts were quantified with subread 2.0.2 [72]. Differentially expressed

606 genes were determined using DESeq2 1.30.0 [73] with a Wald test, regressing out for the batch factor.
607 Subsequently, genes were filtered based on significance (P-value ≤0.05 and PADJ ≤0.25; for the
608 aneuploid vs. control analysis results were filtered only based on p-value). Pre-ranked gene set
609 enrichment analysis (PreRanked GSEA) was performed to identify enriched pathways [74]. Single cell
610 gene set enrichment analysis (ssGSEA) was performed using GenePatterns [74,75], to compare the
611 expression of specific DNA damage-related signatures across samples. Z-scores were calculated for
612 each gene signature across and plotted as a heatmap. Plots were generated using the Python's
613 'seaborn' library (Van Rossum and Drake, 2009).
614
615 **Kinetics of DNA repair upon exposure to IR**
616 After cell sorting (as described above), aneuploid cycling and arrested cells, together with non-sorted
617 aneuploid cells and euploid controls, were plated on coverslips and incubated overnight. The day
618 after, cells were γ-irradiated (1.25Gy) and fixed for immunofluorescence as indicated above at
619 different timepoints. In order to exclude S phase cells, cells were pulsed with EdU 10μM for 30
620 minutes before fixation. Non-irradiated cells were fixed together with the first timepoint. i.e. 0h post
621 irradiation.
622
623 **Association of DDR gene expression with doubling time**
624 CCLE (Cancer cell line encyclopedia) gene expression data were obtained from DepMap
625 (https://depmap.org/portal/) 22Q1 release [60] and cell line doubling times were obtained from
626 Tsherniak et al. 2017. Cell lines were divided to quartiles according to their doubling time, while
627 ssGSEA scores were generated using the GenePattern platform (https://www.genepattern.org/) [74,75]
628 and compared between the top and bottom quartiles. Statistical analysis (two-tailed Student' t-test)
629 and plotting were performed using GraphPad PRISM v9.3.1.
630
631 **Sample processing for single-cell whole genome sequencing (scWGS)**
632 Cell pellets were resuspended in cell lysis buffer (100mM Tris-HCl pH 7.4, 154mM NaCl, 1mM
633 $CaCl_2$, 500μM $MgCl_2$, 0,2% BSA, 0,1% NP-40, 10μg/ml Hoechst 33358, 2μg/ml propidium iodide
634 in ultra-pure water) and incubated on ice in the dark for 15 minutes to ensure complete lysis. Resulting
635 single nuclei of G1 phase (as determined by Hoechst and PI staining) were sorted into single wells of
636 96 wellplates on a MoFlo Astrios cell sorter (Beckman Coulter) and sorted at -80C until firther
637 processing. Automated library preparation was performed (Bravo Automated Liquid Handling
638 Platform, Agilent Technologies) as previously described [76]. Resulting single-cell libraries were
639 pooled for subsequent sequencing.

640

641 **Data analysis for scWGS**

642 Sequencing was performed using a NextSeq 500 machine (Illumina; up to 77 cycles – single end or
643 up to 68 and 9 cycles – paired end; excluding sample-specific barcodes). Reads were afterwards
644 aligned to the human reference genome (GRCh38/hg38) using Bowtie2 (version 2.2.4 or 2.3.4.1;
645 Langmead and Salzberg 2012). Duplicate reads were marked with BamUtil (version 1.0.3; [77]) or
646 Samtools markdup (version 1.9; [78]. The aligned read data (bam files) were analyzed with a copy
647 number calling algorithm called AneuFinder (https://github.com/ataudt/aneufinder; [79]). Following
648 GC correction and blacklisting of artefact-prone regions (extreme low or high coverage in control
649 samples), libraries were analyzed using the dnacopy and edivisive copy number calling algorithms
650 with variable width bins (average bin size = 1 Mb; step size = 500 kb). Results were afterwards
651 curated by requiring a minimum concordance of 95% between the results of the two algorithms.
652 Libraries with on average less than 10 reads per bin (~ 30,000 reads for a diploid genome) were
653 discarded. A chromosome was classified as aneuploid when at least 95 % of the bins showed a
654 deviation from euploid (deviation from 2-somy). Chromosomes 10 and 12 were excluded for the
655 calculation of whole-genome scores.

656

657 **Quantification and statistical analysis**

658 Statistical analyses were performed using GraphPad Prism software. Statistical significance in each
659 case was calculated using Student's t-test, Chi-squared test or Fisher's exact test. Error bars represent
660 SEMs or SDs. All experiments were performed in at least three biological replicates, with some
661 exceptions (see Figure legends).

662

663 ## References

664 1. Santaguida S, Amon A. Short- and long-term effects of chromosome mis-segregation and
665 aneuploidy. *Nat Rev Mol Cell Biol*. 2015;16(8):473-485. doi:10.1038/nrm4025
666 2. Levine MS, Holland AJ. The impact of mitotic errors on cell proliferation and tumorigenesis.
667 *Genes Dev*. 2018;32(9-10):620-638. doi:10.1101/gad.314351.118
668 3. Ben-David U, Amon A. Context is everything: aneuploidy in cancer. *Nat Rev Genet*.
669 2020;21(1):44-62. doi:10.1038/s41576-019-0171-x
670 4. Al-rawi DH, Bakhoum SF. Chromosomal instability as a source of genomic plasticity. *Curr*
671 *Opin Genet Dev*. 2022;74:101913. doi:10.1016/j.gde.2022.101913
672 5. Ippolito MR, Martis V, Martin S, et al. Gene copy-number changes and chromosomal
673 instability induced by aneuploidy confer resistance to chemotherapy. *Dev Cell*.

674 2021;56(17):2440-2454.e6. doi:10.1016/j.devcel.2021.07.006
675 6. Lukow DA, Sausville EL, Suri P, et al. Chromosomal instability accelerates the evolution of
676 resistance to anti-cancer therapies. *Dev Cell*. 2021;56(17):2427-2439.e4.
677 doi:10.1016/j.devcel.2021.07.009
678 7. Shoshani O, Bakker B, De Haan L, et al. Transient genomic instability drives tumorigenesis
679 through accelerated clonal evolution. *Genes Dev*. 2021;35(15-16):1093-1109.
680 doi:10.1101/gad.348319.121
681 8. Trakala M, Aggarwal M, Sniffen C, et al. Clonal selection of stable aneuploidies in
682 progenitor cells drives high-prevalence tumorigenesis. *Genes Dev*. 2021;35(15-16):1079-
683 1092. doi:10.1101/gad.348341.121
684 9. Vasudevan A, Baruah PS, Smith JC, et al. Single-Chromosomal Gains Can Function as
685 Metastasis Suppressors and Promoters in Colon Cancer. *Dev Cell*. 2020;52(4):413-428.e6.
686 doi:10.1016/j.devcel.2020.01.034
687 10. Ohashi A, Ohori M, Iwai K, et al. Aneuploidy generates proteotoxic stress and DNA damage
688 concurrently with p53-mediated post-mitotic apoptosis in SAC-impaired cells. *Nat Commun*.
689 2015;6. doi:10.1038/ncomms8668
690 11. Santaguida S, Vasile E, White E, Amon A. Aneuploidy-induced cellular stresses limit
691 autophagic degradation. *Genes Dev*. 2015;29(19):2010-2021. doi:10.1101/gad.269118.115
692 12. Stingele S, Stoehr G, Peplowska K, Cox J, Mann M, Storchova Z. Global analysis of
693 genome, transcriptome and proteome reveals the response to aneuploidy in human cells. *Mol*
694 *Syst Biol*. 2012;8(608). doi:10.1038/msb.2012.40
695 13. Williams BR, Prabhu VR, Hunter KE, et al. and Spontaneous Immortalization. *October*.
696 2008;322(October):703-710.
697 14. Torres EM, Sokolsky T, Tucker CM, et al. Effects of aneuploidy on cellular physiology and
698 cell division in haploid yeast. *Science (80-)*. 2007;317(5840):916-924.
699 doi:10.1126/science.1142210
700 15. Sheltzer JM, Blank HM, Pfau SJ, et al. Aneuploidy drives genomic instability in yeast.
701 *Science (80-)*. 2011;333(6045):1026-1030. doi:10.1126/science.1206412
702 16. Zhu J, Pavelka N, Bradford WD, Rancati G, Li R. Karyotypic determinants of chromosome
703 instability in Aneuploid budding yeast. *PLoS Genet*. 2012;8(5).
704 doi:10.1371/journal.pgen.1002719
705 17. Passerini V, Ozeri-Galai E, De Pagter MS, et al. The presence of extra chromosomes leads to
706 genomic instability. *Nat Commun*. 2016;7. doi:10.1038/ncomms10754
707 18. Santaguida S, Richardson A, Iyer DR, et al. Chromosome Mis-segregation Generates Cell-

708 Cycle-Arrested Cells with Complex Karyotypes that Are Eliminated by the Immune System.
709 *Dev Cell*. 2017;41(6):638-651.e5. doi:10.1016/j.devcel.2017.05.022
710 19. Davoli T, Xu AW, Mengwasser KE, et al. XCumulative haploinsufficiency and
711 triplosensitivity drive aneuploidy patterns and shape the cancer genome. *Cell*.
712 2013;155(4):948. doi:10.1016/j.cell.2013.10.011
713 20. Garribba L, Santaguida S. The Dynamic Instability of the Aneuploid Genome. *Front Cell*
714 *Dev Biol*. 2022;10. doi:10.3389/fcell.2022.838928
715 21. Blank HM, Sheltzer JM, Meehl CM, Amon A. Mitotic entry in the presence of DNA damage
716 is a widespread property of aneuploidy in yeast. *Mol Biol Cell*. 2015;26(8):1440-1451.
717 doi:10.1091/mbc.E14-10-1442
718 22. Burrell RA, McClelland SE, Endesfelder D, et al. Replication stress links structural and
719 numerical cancer chromosomal instability. *Nature*. 2013;494(7438):492-496.
720 doi:10.1038/nature11935
721 23. Nawata H, Kashino G, Tano K, et al. Dysregulation of gene expression in the artificial
722 human trisomy cells of chromosome 8 associated with transformed cell phenotypes. *PLoS*
723 *One*. 2011;6(9). doi:10.1371/journal.pone.0025319
724 24. Nicholson JM, Macedo JC, Mattingly AJ, et al. Chromosome mis-segregation and
725 cytokinesis failure in trisomic human cells. *Elife*. 2015;4(MAY):1-23.
726 doi:10.7554/eLife.05068
727 25. Wang RW, Viganò S, Ben-David U, Amon A, Santaguida S. Aneuploid senescent cells
728 activate NF-κB to promote their immune clearance by NK cells. *EMBO Rep*. 2021;22(8):1-
729 16. doi:10.15252/embr.202052032
730 26. Lee AJX, Endesfelder D, Rowan AJ, et al. Chromosomal instability confers intrinsic
731 multidrug resistance. *Cancer Res*. 2011;71(5):1858-1870. doi:10.1158/0008-5472.CAN-10-
732 3604
733 27. Cohen-Sharir Y, McFarland JM, Abdusamad M, et al. Aneuploidy renders cancer cells
734 vulnerable to mitotic checkpoint inhibition. *Nature*. 2021;590(7846):486-491.
735 doi:10.1038/s41586-020-03114-6
736 28. Replogle JM, Zhou W, Amaro AE, et al. Aneuploidy increases resistance to
737 chemotherapeutics by antagonizing cell division. *Proc Natl Acad Sci U S A*.
738 2020;117(48):30566-30576. doi:10.1073/pnas.2009506117
739 29. Santaguida S, Tighe A, D'Alise AM, Taylor SS, Musacchio A. Dissecting the role of MPS1
740 in chromosome biorientation and the spindle checkpoint through the small molecule inhibitor
741 reversine. *J Cell Biol*. 2010;190(1):73-87. doi:10.1083/jcb.201001036

742 30. Neelsen KJ, Lopes M. Replication fork reversal in eukaryotes: From dead end to dynamic
743 response. *Nat Rev Mol Cell Biol*. 2015;16(4):207-220. doi:10.1038/nrm3935
744 31. Iyer DR, Rhind N. *Replication Fork Slowing and Stalling Are Distinct, Checkpoint-*
745 *Independent Consequences of Replicating Damaged DNA*. Vol 13.; 2017.
746 doi:10.1371/journal.pgen.1006958
747 32. Lamm N, Ben-David U, Golan-Lev T, Storchová Z, Benvenisty N, Kerem B. Genomic
748 Instability in Human Pluripotent Stem Cells Arises from Replicative Stress and Chromosome
749 Condensation Defects. *Cell Stem Cell*. 2016;18(2):253-261. doi:10.1016/j.stem.2015.11.003
750 33. Ge XQ, Jackson DA, Blow JJ. Dormant origins licensed by excess Mcm2-7 are required for
751 human cells to survive replicative stress. *Genes Dev*. 2007;21(24):3331-3341.
752 doi:10.1101/gad.457807
753 34. Jares P, Blow JJ. Xenopus Cdc7 function is dependent on licensing but not on XORC,
754 XCdc6, or CDK activity and is required for XCdc45 loading. *Genes Dev*. 2000;14(12):1528-
755 1540. doi:10.1101/gad.14.12.1528
756 35. Tanaka S, Umemori T, Hirai K, Muramatsu S, Kamimura Y, Araki H. CDK-dependent
757 phosphorylation of Sld2 and Sld3 initiates DNA replication in budding yeast. *Nature*.
758 2007;445(7125):328-332. doi:10.1038/nature05465
759 36. Labib K. Howdo Cdc7 and cyclin-dependent kinases trigger the initiation of chromosome
760 replication in eukaryotic cells? *Genes Dev*. 2010;24(12):1208-1219.
761 doi:10.1101/gad.1933010
762 37. Heller RC, Kang S, Lam WM, Chen S, Chan CS, Bell SP. Eukaryotic origin-dependent DNA
763 replication in vitro reveals sequential action of DDK and S-CDK kinases. *Cell*.
764 2011;146(1):80-91. doi:10.1016/j.cell.2011.06.012
765 38. Koltun ES, Tsuhako AL, Brown DS, et al. Discovery of XL413, a potent and selective CDC7
766 inhibitor. *Bioorganic Med Chem Lett*. 2012;22(11):3727-3731.
767 doi:10.1016/j.bmcl.2012.04.024
768 39. Zeman MK, Cimprich KA. Causes and consequences of replication stress. *Nat Cell Biol*.
769 2014;16(1):2-9. doi:10.1038/ncb2897
770 40. Chan KL, Palmai-Pallag T, Ying S, Hickson ID. Replication stress induces sister-chromatid
771 bridging at fragile site loci in mitosis. *Nat Cell Biol*. 2009;11(6):753-760.
772 doi:10.1038/ncb1882
773 41. Mankouri HW, Huttner D, Hickson ID. How unfinished business from S-phase affects
774 mitosis and beyond. *EMBO J*. 2013;32(20):2661-2671. doi:10.1038/emboj.2013.211
775 42. Wilhelm T, Olziersky AM, Harry D, et al. Mild replication stress causes chromosome mis-

776 segregation via premature centriole disengagement. *Nat Commun*. 2019;10(1):1-14.
777 doi:10.1038/s41467-019-11584-0
778 43. Ellison V, Stillman B. Biochemical characterization of DNA damage checkpoint complexes:
779 Clamp loader and clamp complexes with specificity for 5′ recessed DNA. *PLoS Biol*.
780 2003;1(2). doi:10.1371/journal.pbio.0000033
781 44. Minocherhomji S, Ying S, Bjerregaard VA, et al. Replication stress activates DNA repair
782 synthesis in mitosis. *Nature*. 2015;528(7581):286-290. doi:10.1038/nature16139
783 45. Baranovskiy AG, Babayeva ND, Suwa Y, Gu J, Pavlov YI, Tahirov TH. Structural basis for
784 inhibition of DNA replication by aphidicolin. *Nucleic Acids Res*. 2014;42(22):14013-14021.
785 doi:10.1093/nar/gku1209
786 46. Bhowmick R, Minocherhomji S, Hickson ID. RAD52 Facilitates Mitotic DNA Synthesis
787 Following Replication Stress. *Mol Cell*. 2016;64(6):1117-1126.
788 doi:10.1016/j.molcel.2016.10.037
789 47. Garribba L, Bjerregaard VA, Gonçalves Dinis MM, et al. Folate stress induces SLX1- And
790 RAD51-dependent mitotic DNA synthesis at the fragile X locus in human cells. *Proc Natl*
791 *Acad Sci U S A*. 2020;117(28):16527-16536. doi:10.1073/pnas.1921219117
792 48. Bonner WM, Redon CE, Dickey JS, et al. γH2AX and cancer. *Nat Rev Cancer*.
793 2008;8(12):957-967. doi:10.1038/nrc2523
794 49. Fenech M, Morley AA. Measurement of micronuclei in lymphocytes. *Mutat Res*. 147(1-
795 2):29-36. doi:10.1016/0165-1161(85)90015-9
796 50. Miura T, Blakely WF. Optimization of calyculin A-induced premature chromosome
797 condensation assay for chromosome aberration studies. *Cytom Part A*. 2011;79 A(12):1016-
798 1022. doi:10.1002/cyto.a.21154
799 51. Xing M, Zhang F, Liao H, et al. Replication Stress Induces ATR/CHK1-Dependent
800 Nonrandom Segregation of Damaged Chromosomes. *Mol Cell*. 2020;78(4):714-724.e5.
801 doi:10.1016/j.molcel.2020.04.005
802 52. Cairns J. Mutation selection and the natural history of cancer. *Nature*. 1975;255(5505):197-
803 200. doi:10.1038/255197a0
804 53. Rocheteau P, Gayraud-Morel B, Siegl-Cachedenier I, Blasco MA, Tajbakhsh S. A
805 subpopulation of adult skeletal muscle stem cells retains all template DNA strands after cell
806 division. *Cell*. 2012;148(1-2):112-125. doi:10.1016/j.cell.2011.11.049
807 54. Dimri GP, Lee X, Basile G, et al. A biomarker that identifies senescent human cells in
808 culture and in aging skin in vivo. *Proc Natl Acad Sci U S A*. 1995;92(20):9363-9367.
809 doi:10.1073/pnas.92.20.9363

810 55. Campisi J, D'Adda Di Fagagna F. Cellular senescence: When bad things happen to good
811 cells. *Nat Rev Mol Cell Biol*. 2007;8(9):729-740. doi:10.1038/nrm2233
812 56. Macedo JC, Vaz S, Bakker B, et al. FoxM1 repression during human aging leads to mitotic
813 decline and aneuploidy-driven full senescence. *Nat Commun*. 2018;9(1):1-17.
814 doi:10.1038/s41467-018-05258-6
815 57. Sakaue-Sawano A, Kurokawa H, Morimura T, et al. Visualizing Spatiotemporal Dynamics of
816 Multicellular Cell-Cycle Progression. *Cell*. 2008;132(3):487-498.
817 doi:10.1016/j.cell.2007.12.033
818 58. Zerbib J, Ippolito MR, Reuveni E, et al. Aneuploid cells depend on the RAF/MEK/ERK
819 pathway and on RNA degradation for overcoming DNA damage and transcriptional burden.
820 *In_Submission*.
821 59. Tsherniak A, Vazquez F, Montgomery PG, et al. Defining a Cancer Dependency Map. *Cell*.
822 2017;170(3):564-576.e16. doi:10.1016/j.cell.2017.06.010
823 60. Ghandi M, Huang FW, Jané-Valbuena J, et al. Next-generation characterization of the
824 Cancer Cell Line Encyclopedia. *Nature*. 2019;569(7757):503-508. doi:10.1038/s41586-019-
825 1186-3
826 61. Hanahan D. Hallmarks of Cancer: New Dimensions. *Cancer Discov*. 2022;12(1):31-46.
827 doi:10.1158/2159-8290.CD-21-1059
828 62. Gemble S, Wardenaar R, Keuper K, et al. Genetic instability from a single S phase after
829 whole-genome duplication. *Nature*. 2022;604(7904):146-151. doi:10.1038/s41586-022-
830 04578-4
831 63. Fragkos M, Ganier O, Coulombe P, Méchali M. DNA replication origin activation in space
832 and time. *Nat Rev Mol Cell Biol*. 2015;16(6):360-374. doi:10.1038/nrm4002
833 64. Iwai K, Nambu T, Dairiki R, et al. Molecular mechanism and potential target indication of
834 TAK-931, a novel CDC7-selective inhibitor. *Sci Adv*. 2019;5(5). doi:10.1126/sciadv.aav3660
835 65. Pilié PG, Tang C, Mills GB, Yap TA. State-of-the-art strategies for targeting the DNA
836 damage response in cancer. *Nat Rev Clin Oncol*. 2019;16(2):81-104. doi:10.1038/s41571-
837 018-0114-z
838 66. Mazzucco G, Huda A, Galli M, Zanella E, Doksani Y. Purification of mammalian telomeric
839 DNA for single-molecule analysis. *Nat Protoc*. Published online 2022:1-27.
840 doi:10.1038/s41596-022-00684-9
841 67. Kolstø AB. *Genome Instability*. Vol 106.; 1998. doi:10.1111/j.1600-0463.1998.tb05651.x
842 68. Mazzucco G, Huda A, Galli M, et al. Telomere damage induces internal loops that generate
843 telomeric circles. *Nat Commun*. 2020;11(1). doi:10.1038/s41467-020-19139-4

844 69. Garribba L, Wu W, Özer Ö, Bhowmick R, Hickson ID, Liu Y. Inducing and Detecting
845 Mitotic DNA Synthesis at Difficult-to-Replicate Loci. *Methods Enzymol*. 2018;601:45-58.
846 doi:10.1016/bs.mie.2017.11.025
847 70. Yates AD, Achuthan P, Akanni W, et al. Ensembl 2020. *Nucleic Acids Res*.
848 2020;48(D1):D682-D688. doi:10.1093/nar/gkz966
849 71. Dobin A, Davis CA, Schlesinger F, et al. STAR: Ultrafast universal RNA-seq aligner.
850 *Bioinformatics*. 2013;29(1):15-21. doi:10.1093/bioinformatics/bts635
851 72. Liao Y, Smyth GK, Shi W. FeatureCounts: An efficient general purpose program for
852 assigning sequence reads to genomic features. *Bioinformatics*. 2014;30(7):923-930.
853 doi:10.1093/bioinformatics/btt656
854 73. Love MI, Huber W, Anders S. Moderated estimation of fold change and dispersion for RNA-
855 seq data with DESeq2. *Genome Biol*. 2014;15(12):1-21. doi:10.1186/s13059-014-0550-8
856 74. Subramanian A, Tamayo P, Mootha VK, et al. Gene set enrichment analysis: A knowledge-
857 based approach for interpreting genome-wide expression profiles. *Proc Natl Acad Sci U S A*.
858 2005;102(43):15545-15550. doi:10.1073/pnas.0506580102
859 75. Reich M, Liefeld T, Gould J, Lerner J, Tamayo P, Mesirov JP. GenePattern 2.0. *Nat Genet*.
860 2006;38(5):500-501. doi:10.1038/ng0506-500
861 76. van den Bos H, Bakker B, Taudt A, et al. Quantification of Aneuploidy in Mammalian
862 Systems. *Methods Mol Biol*. 2019;1896:159-190. doi:10.1007/978-1-4939-8931-7_15
863 77. Jun G, Wing MK, Abecasis GR, Kang HM. An efficient and scalable analysis framework for
864 variant extraction and refinement from population-scale DNA sequence data. *Genome Res*.
865 2015;25(6):918-925. doi:10.1101/gr.176552.114
866 78. Danecek P, Bonfield JK, Liddle J, et al. Twelve years of SAMtools and BCFtools.
867 *Gigascience*. 2021;10(2):1-4. doi:10.1093/gigascience/giab008
868 79. Bakker B, Taudt A, Belderbos ME, et al. Single-cell sequencing reveals karyotype
869 heterogeneity in murine and human malignancies. *Genome Biol*. 2016;17(1):1-15.
870 doi:10.1186/s13059-016-0971-7
871 80. Zhang CZ, Spektor A, Cornils H, et al. Chromothripsis from DNA damage in micronuclei.
872 *Nature*. 2015;522(7555):179-184. doi:10.1038/nature14493
873

874 **Acknowledgments**

875 We are very grateful to all the members of the Santaguida group for fruitful discussions throughout
876 the project. We thank Elsa Logarinho and members of M. Mapelli lab for constructive discussions.
877 Work in the Santaguida lab is supported by grants from the Italian Association for Cancer Research

(MFAG 2018 - ID. 21665 project), Ricerca Finalizzata (GR-2018-12367077), Fondazione Cariplo, the Rita-Levi Montalcini program from MIUR and the Italian Ministry of Health with Ricerca Corrente and 5x1000 funds. L.G. is supported by a fellowship from Fondazione IEO-Monzino. Work in the Ben-David lab is supported by grants from the European Research Council (ERC grant #945674), Israel Cancer Research Foundation Gesher Award, Israel Science Foundation (ISF grant #1805/21), the DoD CDMRP Career Development Award (grant #CA191148), the Azrieli Faculty Fellowship and the EMBO Young Investigator Program.

Figure legends

Fig. 1: Aneuploid cells accumulate increasing genome instability and display higher levels of DNA replication stress markers in S phase. a, Experimental setup for the analysis of genome instability of cells obtained from the 1st and the 2nd mitosis. Karyotype aberrations were assessed by mFISH analysis. **b,c,** Representative mFISH images of karyotypes obtained from the 1st and the 2nd mitosis in aneuploid cells and relative quantification. T(10,X) and +12 were excluded from the analysis as they are clonal in hTERT RPE-1 cells. **d,** Schematic representation of the experimental approaches used for the study of the 1st S phase after induction of chromosome missegregation. A short EdU pulse was performed before cell harvest in order to label S phase cells to be analyzed by immunofluorescence. **e,f,** Representative images of normal and reversed replication forks analyzed by electron microscopy and quantification of the reversed ones in control and aneuploid cells. 108 and 95 forks were analyzed in the control and in the aneuploid sample, respectively. **g,h,** Representative images and quantification of FANCD2 foci per S phase cell in control and aneuploid cells. **i,j,** Representative images and quantification of RPA foci per S phase cell in control and aneuploid cells. **k,l,** Representative images and quantification of pChk1 foci per S phase cell in control and aneuploid cells. Cells treated with aphidicolin (RS, replication stress) were used as a positive control. **m,** Representative images of DNA fiber analysis in control and aneuploid cells. **n,o,** Quantification of (**n**) fork density per Mb and (**o**) origin firing rate per Mb in control and aneuploid cells. Ctrl, control (DMSO pulsed). Aneu, aneuploid cells (Mps1 inhibitor pulsed). RS, replication stress (aphidicolin treated cells). Scale bars, 5μm. LUT was inverted for FANCD2, RPA and pChk1 images. Data are means of at least three biological replicates, except for the EM (one replicate) and the DNA combing (two replicates) analyses. Error bars represent SEMs. ** denotes $p<0,01$; **** denotes $p <0,001$.

Fig. 2: DDK protects aneuploid cells from DNA damage accumulation and consequent cell death. a, Experimental workflow for the analysis of DNA replication stress markers in S phase cells

912 upon treatment with the DDK inhibitor XL-413. A short EdU pulse was performed before cell harvest
913 in order to label S phase cells. **b,c,** Representative images and quantification of FANCD2 foci per S
914 phase cell in control or aneuploid cells ± DDK inhibitor. **d,e,** Representative images and
915 quantification of RPA foci per S phase cell in control or aneuploid cells ± DDK inhibitor. **f,g,**
916 Representative images and quantification of pChk1 foci per S phase cell in control or aneuploid cells
917 ± DDK inhibitor. **h,** Experimental workflow for the assessment of cell viability upon exposure to the
918 DDK inhibitor. **i,** Quantification of live cells upon DDK inhibitor treatment in control and aneuploid
919 cells. Ctrl, control (DMSO pulsed). Aneu, aneuploid cells (Mps1 inhibitor pulsed). DDKi, DDK
920 inhibitor. Scale bars, 5μm. LUT was inverted for FANCD2, RPA and pChk1 images. Data are means
921 of at least three biological replicates. Error bars represent SEMs. * denotes p<0,05; ** denotes
922 p<0,01; *** denotes p< 0,005; **** denotes p<0,001.
923
924 **Fig. 3: MiDAS protects aneuploid cells from a further increase in their genome instability. a,**
925 Experimental workflow for the analysis of the 1st S phase duration, 2nd M phase duration and quality
926 by live-cell imaging in hTERT RPE-1 cells expressing H2b-RFP and PCNA-GFP. **b,** Representative
927 images from the movies of mitosis duration and quality in control and aneuploid cells. **c,d,** Correlation
928 between (**c**) S phase duration and quality of the subsequent mitosis and (**d**) mitotic timing and mitotic
929 quality in control and aneuploid cells. **e,f**, Representative images and quantification of EdU
930 incorporation on metaphase spreads in control and aneuploid cells. Cells treated with aphidicolin (RS,
931 replication stress) were used as a positive control. **g,** Experimental workflow for the assessment of
932 genome instability in the following G1 phase upon MiDAS inhibition. **h,i,** Representative images and
933 quantification of EdU incorporation in prometaphase cells upon MiDAS inhibition. Cells treated with
934 aphidicolin (RS, replication stress) were used as a positive control. **j,k,l,** Representative images (**j**)
935 and quantification of 53BP1 body (**k**) and micronucleus (**l**) accumulation in G1 cells following
936 inhibition of MiDAS. Ctrl, control (DMSO pulsed). Aneu, aneuploid cells (Mps1 inhibitor pulsed).
937 RS, replication stress (aphidicolin treated cells). MiDASi, MiDAS inhibitor. Normal M, normal
938 mitosis. Abnormal M, abnormal mitosis. Scale bars, 5 or 10 μm. Data are means of at least three
939 biological replicates. Error bars represent SEMs. * denotes p<0,05; **denotes p<0,01; *** denotes
940 p< 0,005; **** denotes p<0,001.
941
942 **Fig. 4: DDK and MiDAS act as surveillance mechanisms to limit genome instability**
943 **accumulation in aneuploid cells. a**, Experimental workflow for the analysis of DNA damage and
944 chromosome aberrations in G1 cells following DDK and MiDAS inhibition in the cell cycle after
945 chromosome missegregation induction. **b,c,d,** Representative images (**b**) and quantification of

946 FANCD2 (**c**) and γH2AX (**d**) accumulation in cytokinesis-blocked pseudo-G1 cells expressing LCK-
947 GFP. **e**, Representative mFISH images of G1 cell-derived metaphase-like chromosomes from
948 aneuploid cells upon DDK and MiDAS inhibition. **f**, Zoomed image of the chromosome highlighted
949 in the dotted-line box in panel E (image on the right) from the aneuploid sample in which DDK and
950 MiDAS were inhibited showing a translocation between chromosome 19 and chromosome 18. **g**,
951 Quantification of the percentage of cells with more than 1 translocation in the two samples. **h,i,j**,
952 Representative images (**h**) and quantification of FANCD2 (**i**) and γH2AX (**j**) non-random distribution
953 between the daughter pseudo-G1 cells. Cells treated with aphidicolin (RS, replication stress) were
954 used as a positive control. Ctrl, control (DMSO pulsed). Aneu, aneuploid cells (Mps1 inhibitor
955 pulsed). RS, replication stress (aphidicolin treated cells). MiDASi, MiDAS inhibitor. NDD, non-
956 random distribution. Scale bars, 5 or 10 μm. Data are means of at least three biological replicates,
957 except for data in panels e-g that were obtained from two biological replicates. Error bars represent
958 SEMs. * denotes p<0,05; ** denotes p<0,01; *** denotes p< 0,005; **** denotes p<0,001.
959
960 **Fig. 5: Aneuploid cells that retained their proliferative capacity exhibit reduced levels of DNA**
961 **damage and genome instability. a**, Senescence-associated β-galactosidase staining in control and
962 aneuploid cells. Doxorubicin-treated cells were used as a positive control. **b**, Experimental workflow
963 for a new method to separate and recover both cycling and arrested aneuploid cells based on FACS-
964 sorting and the usage of a fluorescent substrate of the b-galactosidase enzyme. **c**, FACS profiles
965 showing the percentage of DDAOG-positive cells in aneuploid cells incubated or not with the
966 DDAOG substrate. **d**, Senescence-associated β-galactosidase staining in cycling and arrested
967 aneuploid cells obtained after sorting. **e**, Cell cycle profiles of control, aneuploid, aneuploid cycling
968 and aneuploid arrested FUCCI-cells analyzed by live-cell imaging. **f**, Quantification of percentage of
969 G1 cells in the four samples analyzed by live-cell imaging. **g,h,i,** Representative images (**g**) and
970 quantification of FANCD2 (**h**) and γH2AX (**i**) foci per cell in the different samples. Only EdU
971 negative cells were analyzed in order to exclude the contribution of S phase cells present in the non-
972 arrested cell samples. **j**, scWGS of cycling and arrested aneuploid cells. Single cells are represented
973 in rows and chromosomes plotted as columns. Copy-number states are indicated in colors (see legend
974 on the right). hTERT RPE-1 cells have clonal gains of 10q and chromosome 12 [80]. **k,** Quantification
975 of cells with at least 3 aneuploid chromosomes in the two samples. Gains of 10q and chromosome 12
976 were excluded from the analysis. Ctrl or Ct, control (DMSO pulsed). Aneu or An, aneuploid cells
977 (Mps1 inhibitor pulsed). Aneu cycling or An cy, aneuploid cycling cells. Aneu arrested or An ar,
978 aneuploid arrested cells. Scale bars, 5μm. Data are means of at least three biological replicates, except

979 for panel f (one replicate). Error bars represent SEMs, except for panel E (SDs). * denotes p<0,05;
980 **** denotes p<0,001.
981
982 **Fig. 6: Cycling aneuploid cells display decreased karyotype aberrations and upregulate DNA**
983 **repair genes in comparison with arrested aneuploid cells. a**, Experimental workflow for the
984 assessment of genome instability levels by live-cell imaging in aneuploid cycling cells expressing
985 H2b-GFP. **b**, Representative images of cell divisions in the different samples. **c**, Quantification of
986 mitotic errors in 3 cell division rounds in control and aneuploid cycling cells. Cells treated with the
987 Mps1 inhibitor just before starting the time-lapse were used as a positive control for mitotic errors.
988 **d**, Volcano plot illustrating the differentially expressed pathways between cycling and arrested
989 aneuploid cells. Specific gene sets are highlighted in color. **e,** Heat-map showing the z-scores of
990 single-sample GSEA (ssGSEA) scores for DNA damage-related gene sets. **f,g,** Quantification of
991 γH2AX foci (f) and 53BP1 bodies (g) in cycling and arrested aneuploid cells upon IR exposure. Only
992 EdU negative cells were analyzed in order to exclude the contribution of S phase cells present in the
993 non-arrested cell samples. **h,i,j,** Association between ssGSEA score for GOBP DNA repair (**h**) or
994 GOBP DNA synthesis involved in DNA repair (**i**) or GOBP regulation of DNA repair (**j**) and
995 proliferation capacity in top vs. bottom quartiles of cancer cell lines from [59]. Aneu cycling or An cy,
996 aneuploid cycling cells. Aneu arrested or An ar, aneuploid arrested cells. M, mother division. D,
997 daughter division. GD, grand-daughter division. Mps1i, Mps1 inhibitor. #1 and #2 refer to biological
998 replicates. Not irrad., not irradiated. Data are means of at least two biological replicates. Error bars
999 represent SEMs. Shaded error bands in panels f,g are shown above and below for arrested and cycling
1000 cells, respectively. **** denotes p<0,001; ns, not significant.
1001
1002 **Fig. 7: Final model.** A model for how aneuploidy induces genome instability and its consequences.
1003 See text for more details.
1004
1005 **Extended Data Fig. 1: Impact of chromosome mis-segregation induction on karyotype changes,**
1006 **S and M phase. a**, Representative images of the karyotype obtained from the 1st and the 2nd mitosis
1007 in control cells. **b**, Quantification of percentage of cells with chromosome gains, losses or
1008 translocations in the 1st or 2nd mitosis in control cells. **c**, Quantification of S phase duration by live-
1009 cell imaging in control and aneuploid cells. The graph refers to the experiment in Figure 3, panels A-
1010 D. **d**, Quantification of mitotic division timing upon SAC inhibition in control and aneuploid cells
1011 that underwent normal or abnormal mitosis. Ctrl, control (DMSO pulsed). Aneu, aneuploid cells

1012 (Mps1 inhibitor pulsed). Mps1i, Mps1 inhibitor. Data are means of at least three biological replicates.
1013 Error bars represent SEMs. *** denotes p<0,005; **** denotes p<0,001.
1014
1015 **Extended Data Fig. 2: Separation and characterization of aneuploid cycling and arrested cells.**
1016 **a**, FACS profiles showing the percentage of DDAOG positive cells in DMSO and doxorubicin treated
1017 cells, used as a positive control. **b,** Illustration depicting the change in nuclear color in the FUCCI
1018 cells. **c**, Representative images showing the starting (0h) and end point (24h) of the time-lapse in the
1019 four different samples. Scale bar 20μm.
1020
1021 **Extended Data Fig. 3: Kinetics of DNA damage repair in aneuploid cells and respective controls**
1022 **upon IR exposure. a,b,** Representative images (**a**) and quantification (**b**) of γH2AX foci per cell.
1023 **c,d,** Representative images (**c**) and quantification (**d**) of 53BP1 bodies per cell. Only EdU negative
1024 cells were analyzed in order to exclude the contribution of S phase cells present in the non-arrested
1025 cell samples. Ctrl, control (DMSO pulsed). Aneu, aneuploid cells (Mps1 inhibitor pulsed). Aneu
1026 cycling, aneuploid cycling cells. Aneu arrested, aneuploid arrested cells. Not irrad., not irradiated.
1027 Data are means of two biological replicates. Shaded error bands in panels f,g are shown above and
1028 below for aneuploid cells and euploid controls, respectively.
1029
1030 **Extended Data Table 1: List of genes differentially expressed in arrested vs. cycling aneuploid**
1031 **cells.** Data were obtained by RNAseq (Fig. 6).
1032
1033
1034
1035
1036

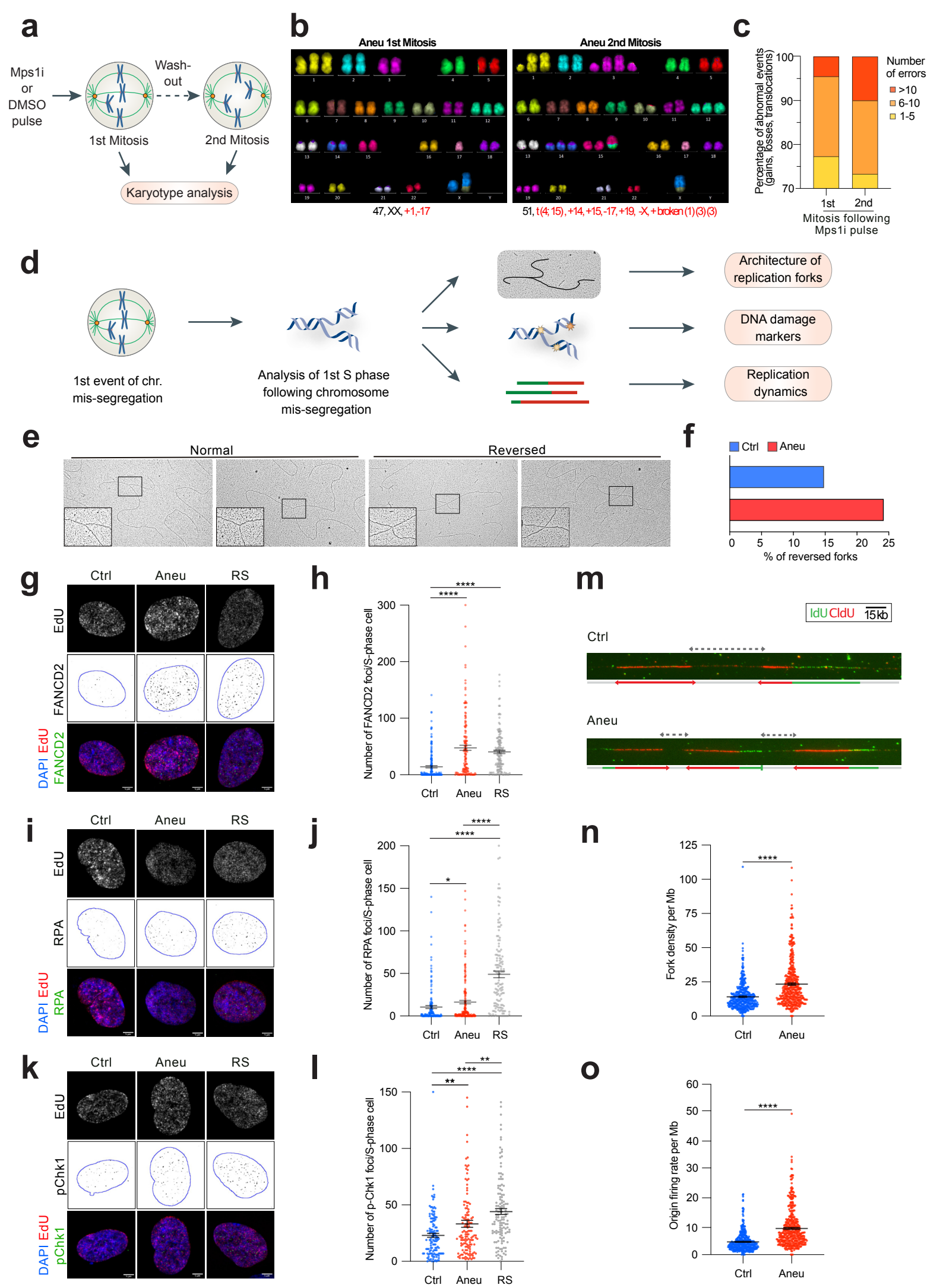
a
Mps1i or DMSO pulse
Wash-out
1st Mitosis
2nd Mitosis
Karyotype analysis
b
Aneu 1st Mitosis
Aneu 2nd Mitosis
47, XX, +1,-17
51, t(4;15), +14, +15, -17, +19, -X, +broken(1)(3)(3)
c
Percentage of abnormal events (gains, losses, translocations)
Number of errors
>10
6-10
1-5
1st
2nd
Mitosis following Mps1i pulse
d
1st event of chr. mis-segregation
Analysis of 1st S phase following chromosome mis-segregation
Architecture of replication forks
DNA damage markers
Replication dynamics
e
Normal
Reversed
f
Ctrl
Aneu
% of reversed forks
g
Ctrl
Aneu
RS
EdU
FANCD2
DAPI EdU FANCD2
h
Number of FANCD2 foci/S-phase cell
m
IdU CldU
15kb
Ctrl
Aneu
i
RPA
DAPI EdU RPA
j
Number of RPA foci/S-phase cell
n
Fork density per Mb
k
pChk1
DAPI EdU pChk1
l
Number of p-Chk1 foci/S-phase cell
o
Origin firing rate per Mb

Figure 1

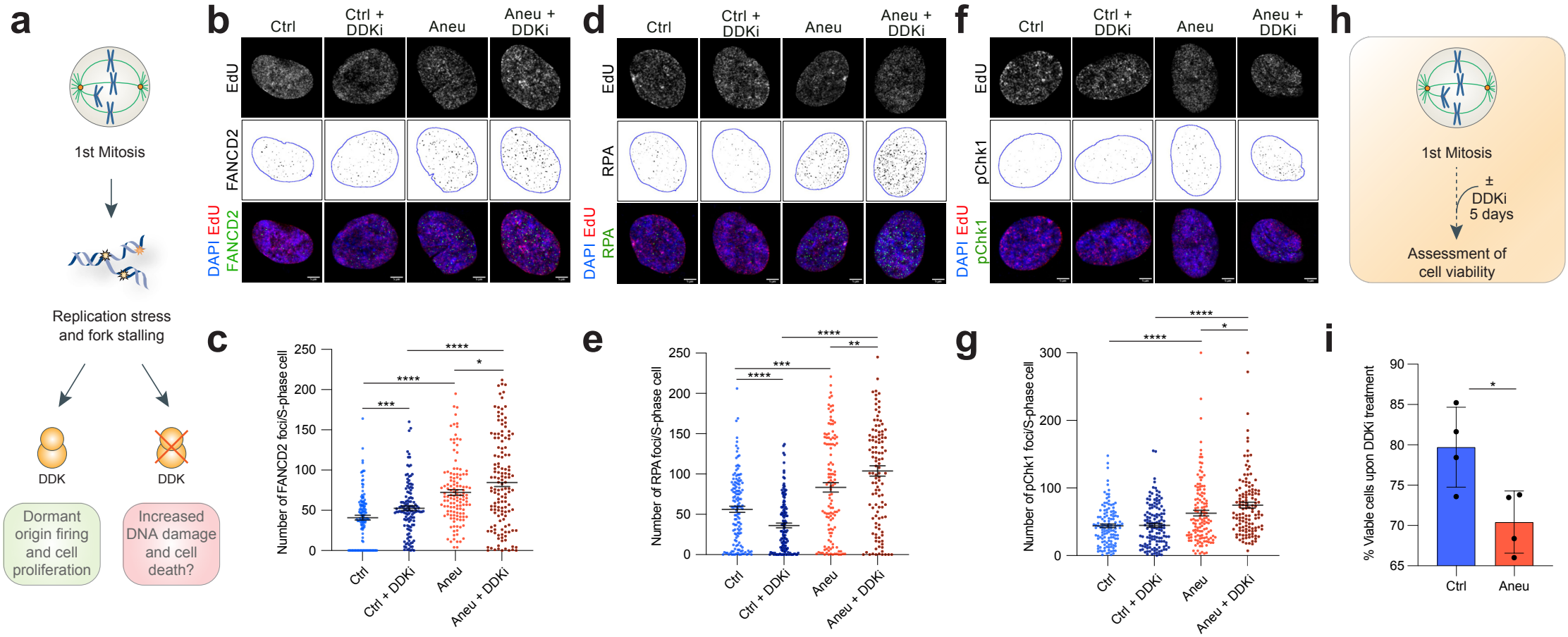
a
1st Mitosis
Replication stress and fork stalling
DDK
DDK
Dormant origin firing and cell proliferation
Increased DNA damage and cell death?
b
Ctrl
Ctrl + DDKi
Aneu
Aneu + DDKi
EdU
FANCD2
DAPI EdU FANCD2
c
Number of FANCD2 foci/S-phase cell
d
RPA
DAPI EdU RPA
e
Number of RPA foci/S-phase cell
f
pChk1
DAPI EdU pChk1
g
Number of pChk1 foci/S-phase cell
h
1st Mitosis
± DDKi 5 days
Assessment of cell viability
i
% Viable cells upon DDKi treatment

Figure 2

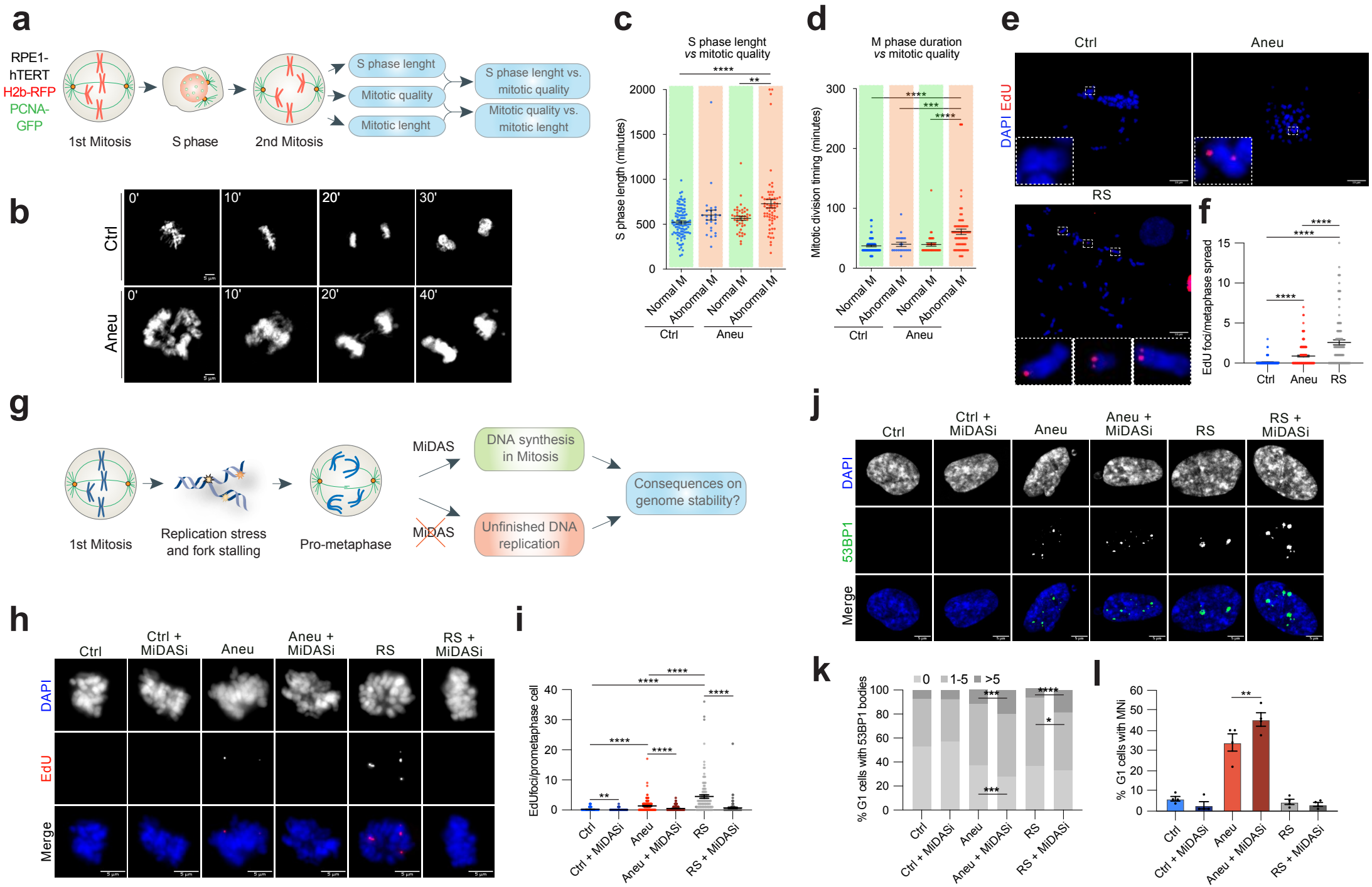
a
RPE1-hTERT
H2b-RFP
PCNA-GFP
1st Mitosis
S phase
2nd Mitosis
S phase lenght
Mitotic quality
Mitotic lenght
S phase lenght vs. mitotic quality
Mitotic quality vs. mitotic lenght
b
Ctrl
Aneu
0'
10'
20'
30'
40'
c
S phase lenght vs mitotic quality
S phase length (minutes)
Normal M
Abnormal M
Ctrl
Aneu
d
M phase duration vs mitotic quality
Mitotic division timing (minutes)
e
Ctrl
Aneu
RS
DAPI EdU
f
EdU foci/metaphase spread
g
1st Mitosis
Replication stress and fork stalling
Pro-metaphase
MiDAS
DNA synthesis in Mitosis
Unfinished DNA replication
Consequences on genome stability?
h
Ctrl
Ctrl + MiDASi
Aneu
Aneu + MiDASi
RS
RS + MiDASi
DAPI
EdU
Merge
i
EdUfoci/prometaphase cell
j
53BP1
k
% G1 cells with 53BP1 bodies
0
1-5
>5
l
% G1 cells with MNi

Figure 3

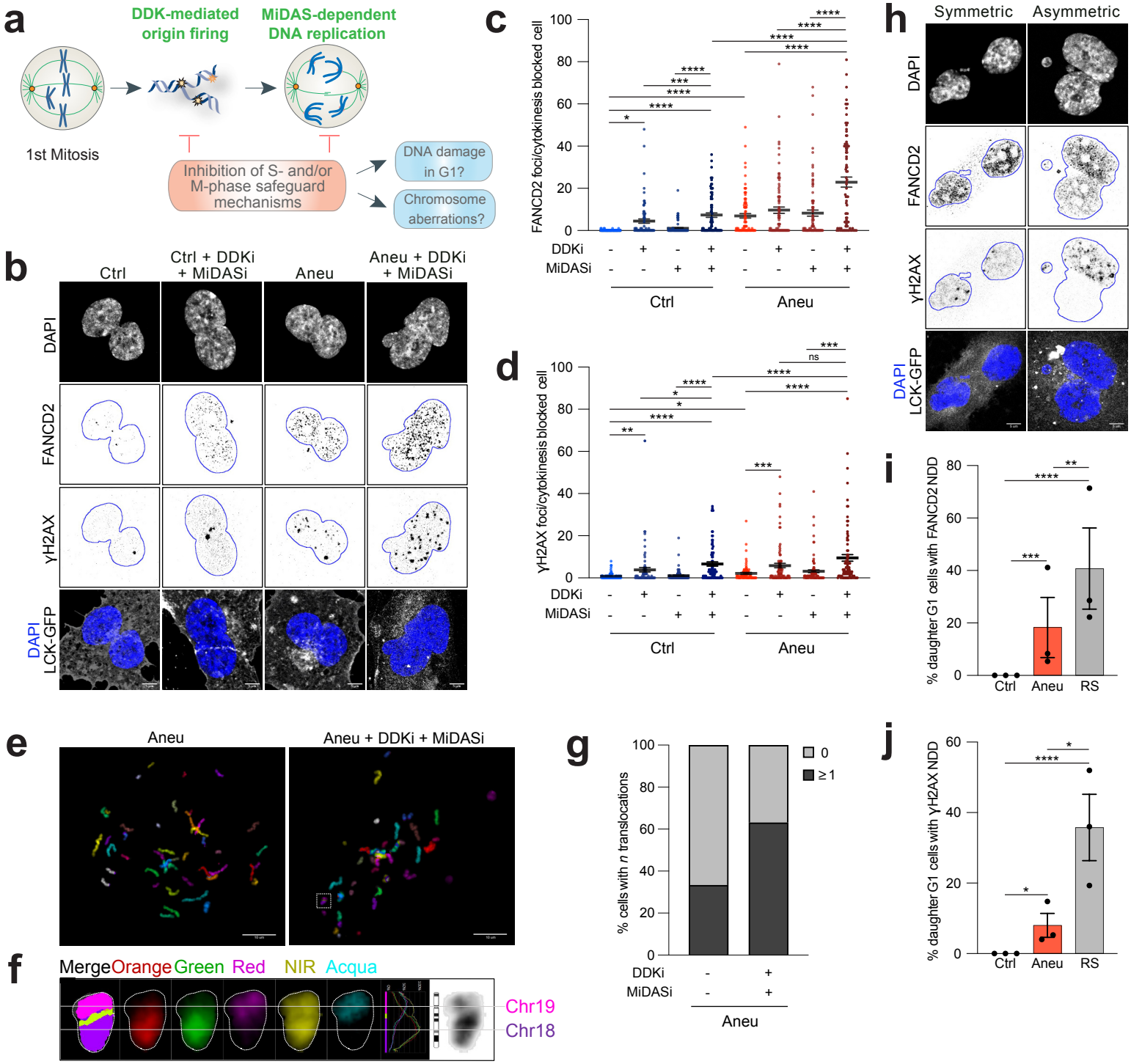
a
DDK-mediated origin firing
MiDAS-dependent DNA replication
1st Mitosis
Inhibition of S- and/or M-phase safeguard mechanisms
DNA damage in G1?
Chromosome aberrations?
b
Ctrl
Ctrl + DDKi + MiDASi
Aneu
Aneu + DDKi + MiDASi
DAPI
FANCD2
γH2AX
DAPI LCK-GFP
c
FANCD2 foci/cytokinesis blocked cell
DDKi
MiDASi
Ctrl
Aneu
d
γH2AX foci/cytokinesis blocked cell
DDKi
MiDASi
Ctrl
Aneu
h
Symmetric
Asymmetric
DAPI
FANCD2
γH2AX
DAPI LCK-GFP
i
% daughter G1 cells with FANCD2 NDD
Ctrl
Aneu
RS
e
Aneu
Aneu + DDKi + MiDASi
f
Merge Orange Green Red NIR Acqua
Chr19
Chr18
g
% cells with n translocations
0
≥ 1
DDKi
MiDASi
Aneu
j
% daughter G1 cells with γH2AX NDD
Ctrl
Aneu
RS

Figure 4

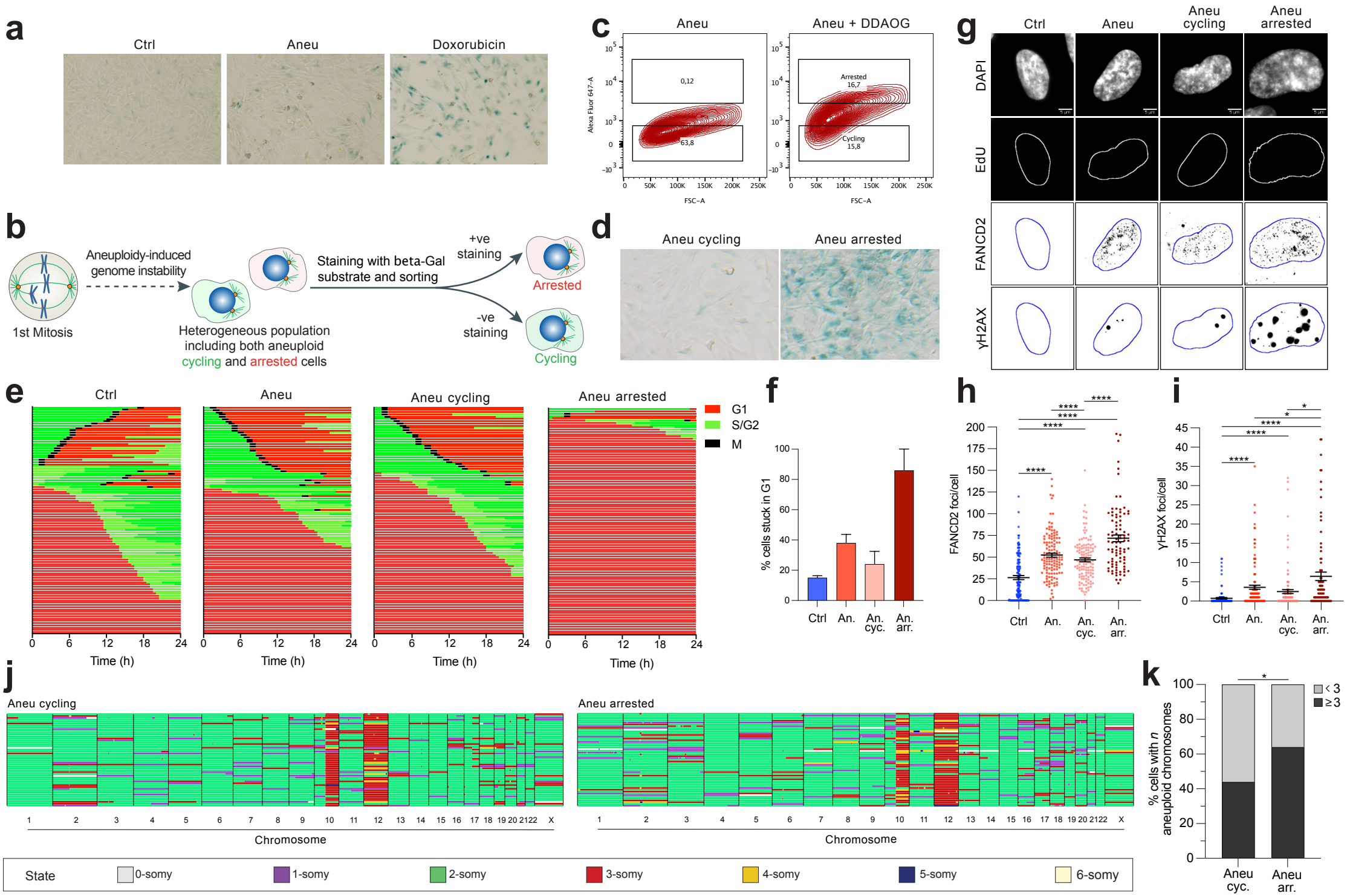
a
Ctrl
Aneu
Doxorubicin
b
1st Mitosis
Aneuploidy-induced genome instability
Heterogeneous population including both aneuploid cycling and arrested cells
Staining with beta-Gal substrate and sorting
+ve staining
-ve staining
Arrested
Cycling
c
Aneu
Aneu + DDAOG
Alexa Fluor 647–A
FSC–A
0,12
63,8
Arrested 16,7
Cycling 15,8
d
Aneu cycling
Aneu arrested
e
Ctrl
Aneu
Aneu cycling
Aneu arrested
G1
S/G2
M
Time (h)
f
% cells stuck in G1
Ctrl
An.
An. cyc.
An. arr.
g
Ctrl
Aneu
Aneu cycling
Aneu arrested
DAPI
EdU
FANCD2
γH2AX
h
FANCD2 foci/cell
i
γH2AX foci/cell
j
Aneu cycling
Aneu arrested
Chromosome
State
0-somy
1-somy
2-somy
3-somy
4-somy
5-somy
6-somy
k
% cells with n aneuploid chromosomes
< 3
≥ 3
Aneu cyc.
Aneu arr.

Figure 5

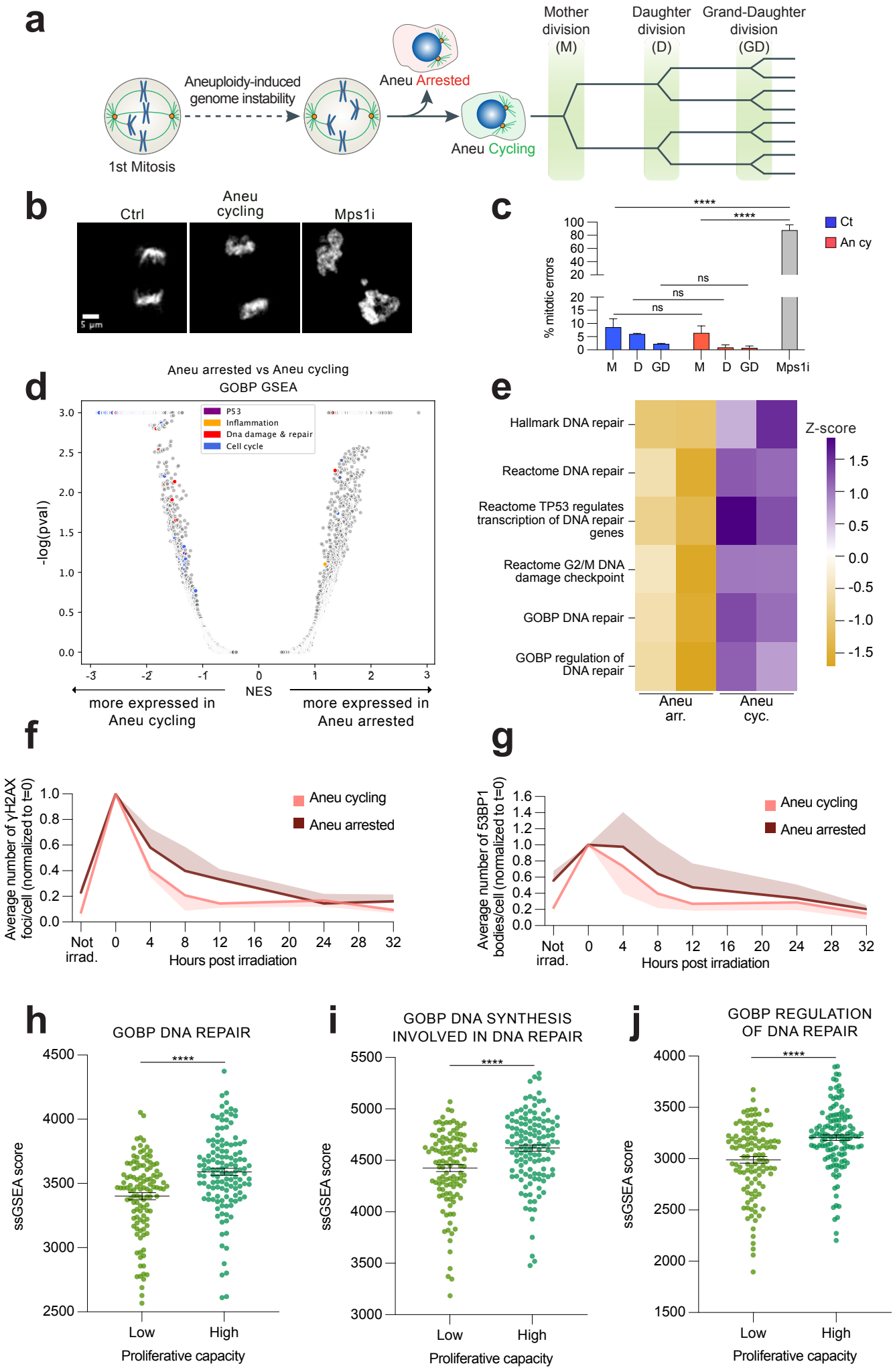
a
1st Mitosis
Aneuploidy-induced genome instability
Aneu Arrested
Aneu Cycling
Mother division (M)
Daughter division (D)
Grand-Daughter division (GD)
b
Ctrl
Aneu cycling
Mps1i
5 µm
c
% mitotic errors
Ct
An cy
****
ns
M
D
GD
Mps1i
d
Aneu arrested vs Aneu cycling
GOBP GSEA
P53
Inflammation
Dna damage & repair
Cell cycle
-log(pval)
NES
more expressed in Aneu cycling
more expressed in Aneu arrested
e
Hallmark DNA repair
Reactome DNA repair
Reactome TP53 regulates transcription of DNA repair genes
Reactome G2/M DNA damage checkpoint
GOBP DNA repair
GOBP regulation of DNA repair
Z-score
Aneu arr.
Aneu cyc.
f
Average number of γH2AX foci/cell (normalized to t=0)
Aneu cycling
Aneu arrested
Not irrad.
Hours post irradiation
g
Average number of 53BP1 bodies/cell (normalized to t=0)
Aneu cycling
Aneu arrested
Not irrad.
Hours post irradiation
h
GOBP DNA REPAIR
ssGSEA score
Low
High
Proliferative capacity
i
GOBP DNA SYNTHESIS INVOLVED IN DNA REPAIR
ssGSEA score
Low
High
Proliferative capacity
j
GOBP REGULATION OF DNA REPAIR
ssGSEA score
Low
High
Proliferative capacity

Figure 6

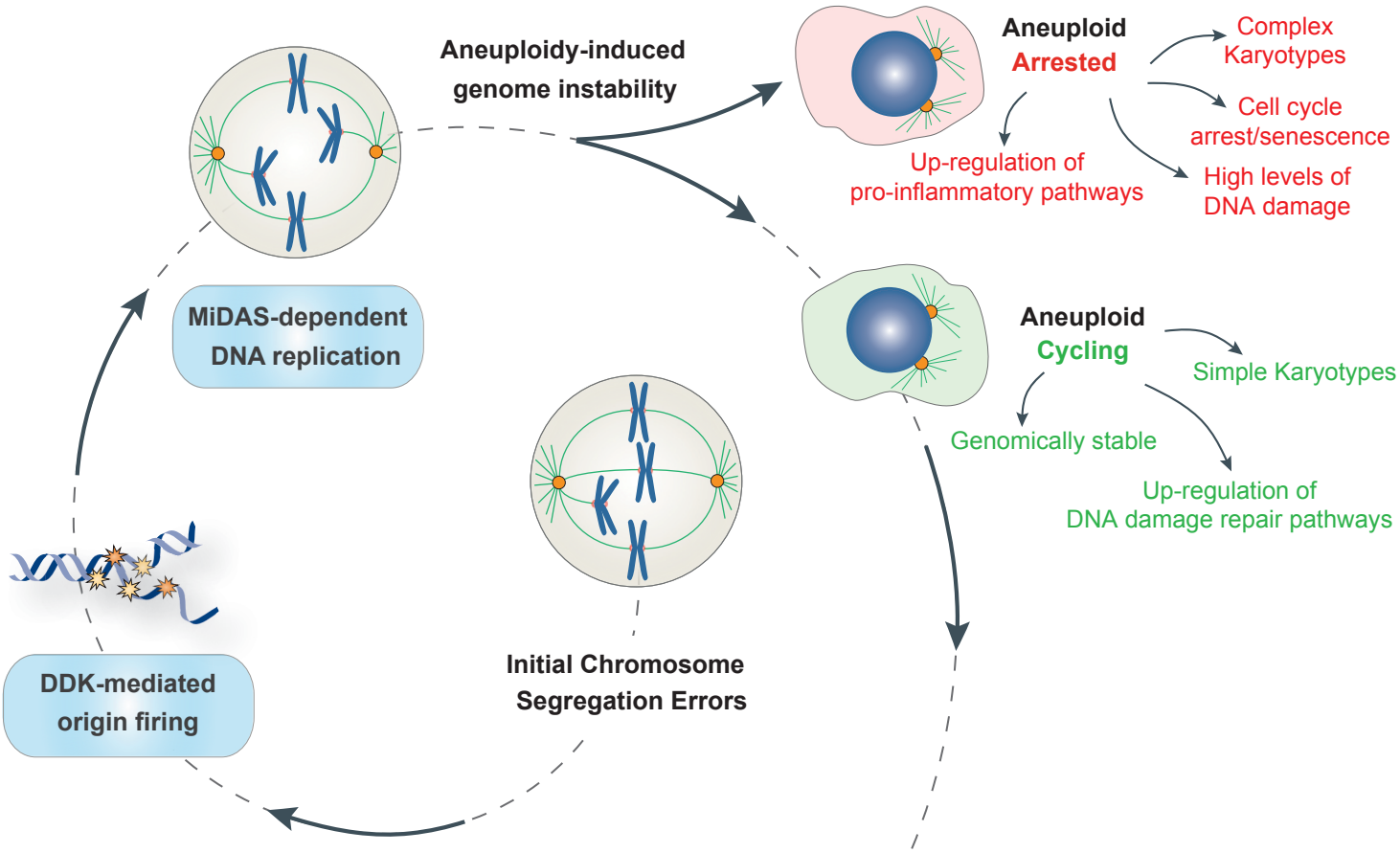
Aneuploidy-induced
genome instability
Aneuploid
Arrested
Complex
Karyotypes
Cell cycle
arrest/senescence
High levels of
DNA damage
Up-regulation of
pro-inflammatory pathways
MiDAS-dependent
DNA replication
Aneuploid
Cycling
Simple Karyotypes
Genomically stable
Up-regulation of
DNA damage repair pathways
Initial Chromosome
Segregation Errors
DDK-mediated
origin firing

Figure 7

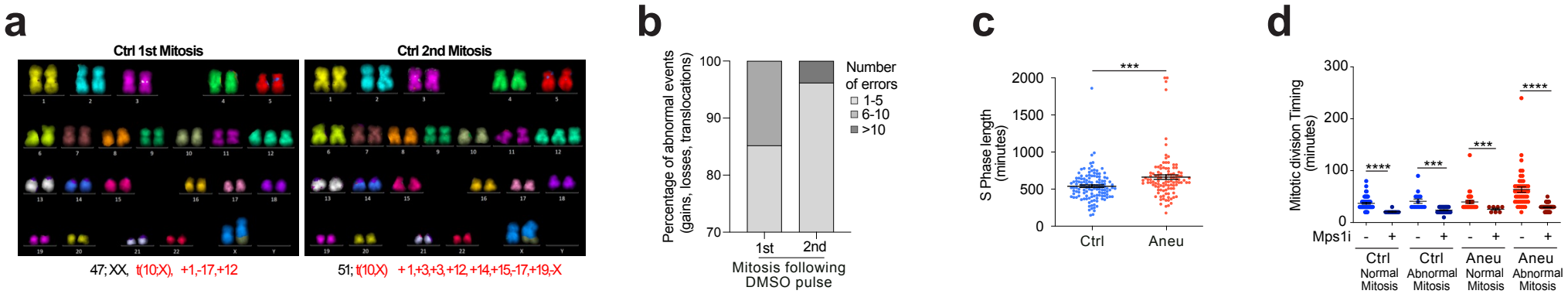

Extended Data Figure 1

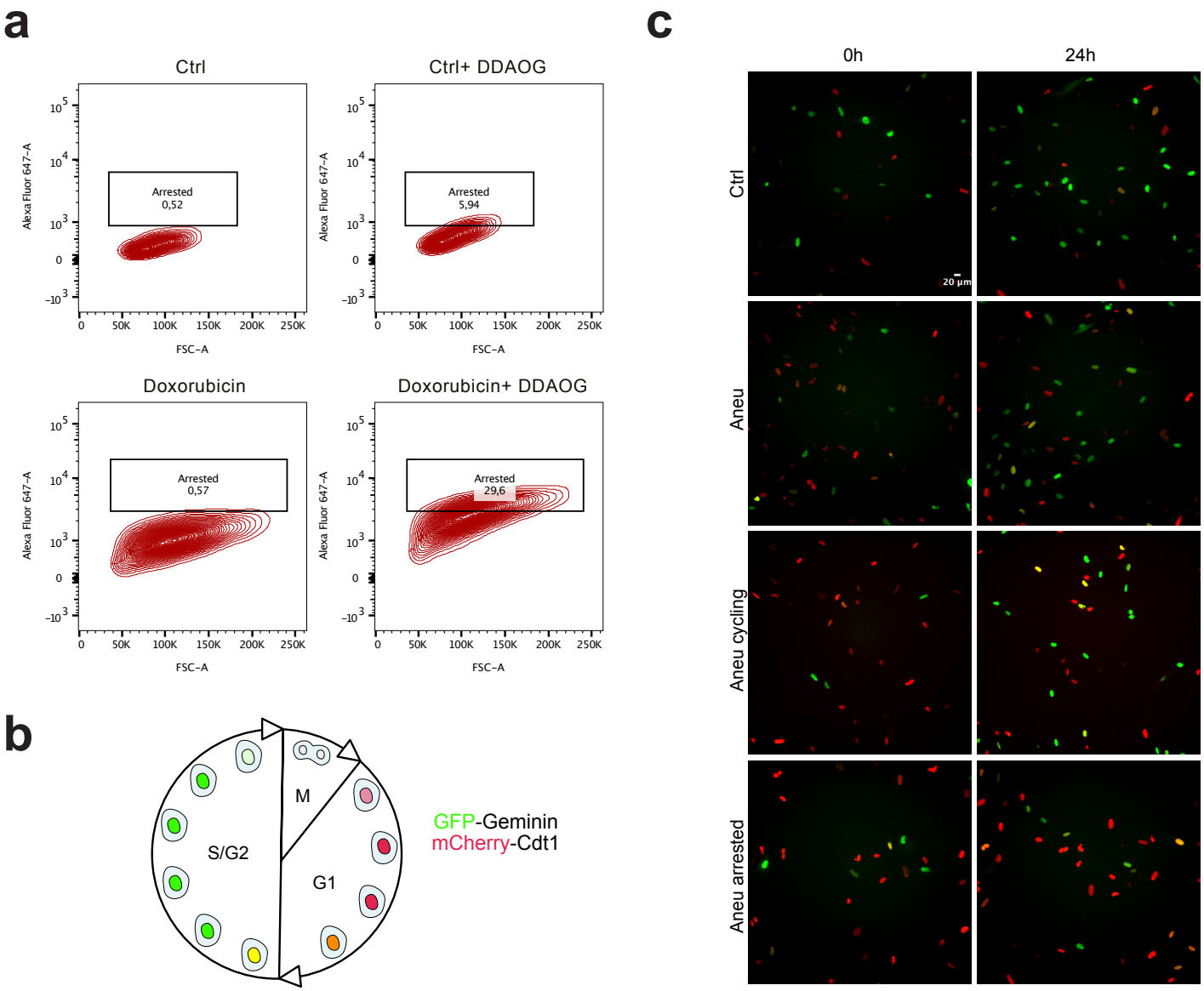

Extended Data Figure 2

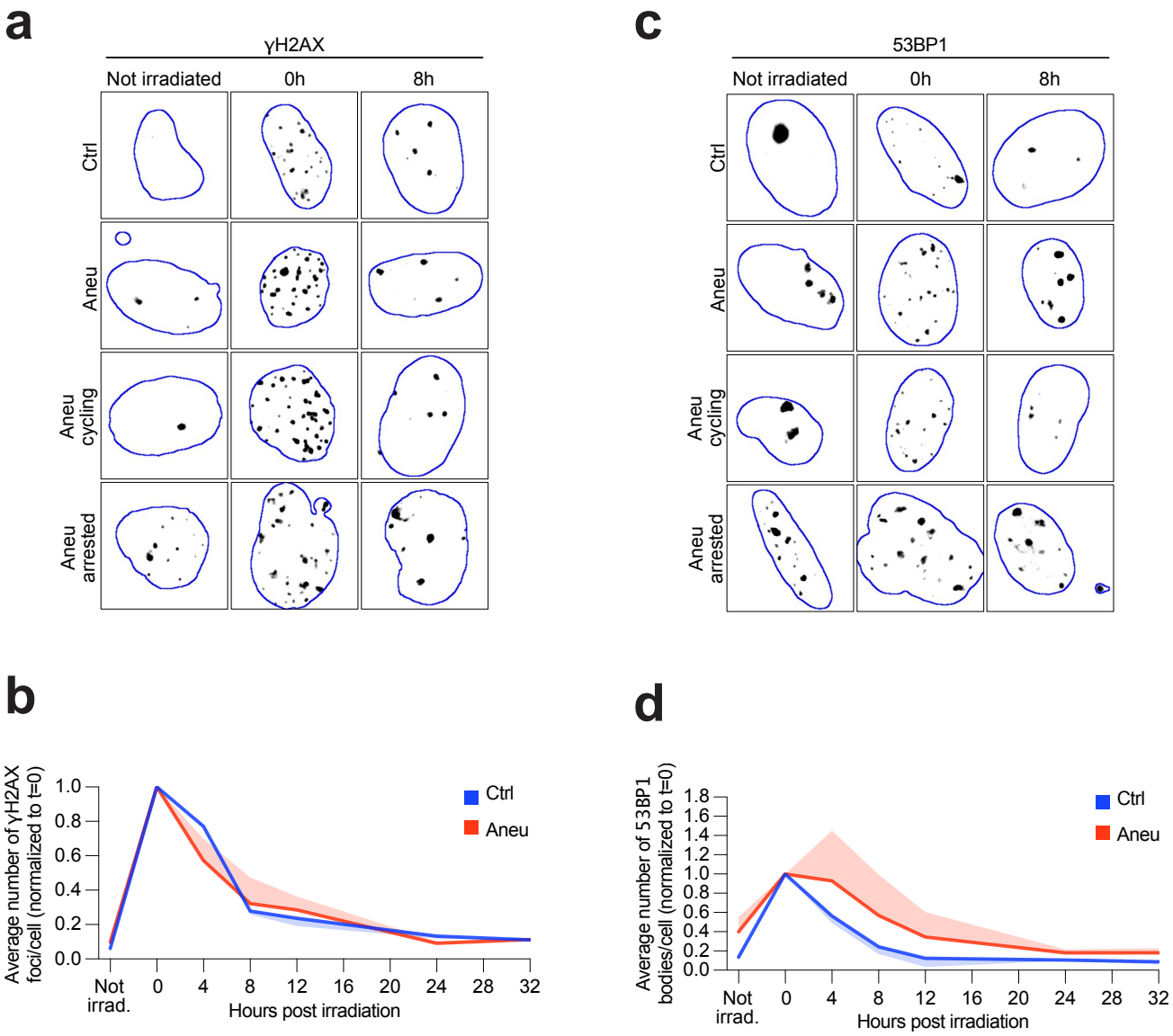

Extended Data Figure 3

gene_name	ensembl_gene_id	baseMean	log2FoldChange	lfcSE	stat	pvalue	padj	signature
UHRF1	ENSG00000276043	992,6407794	-1,463494234	0,23690646	-6,177519319	6,51166E-10	1,46332E-07	GOBP_DNA_REPAIR [569]
FOXM1	ENSG00000111206	1019,397201	-1,365225147	0,581676165	-2,347053616	0,018922532	0,137644121	GOBP_DNA_REPAIR [569]
PRIM1	ENSG00000198056	474,8477874	-1,364119404	0,245844729	-5,548703086	2,87796E-08	3,52553E-06	HALLMARK_DNA_REPAIR [150]
FANCE	ENSG00000112039	267,7712184	-1,343504755	0,283509612	-4,738833176	2,14952E-06	0,000111839	REACTOME_DNA_REPAIR [332]
H2BC14	ENSG00000273703	174,2119743	-1,330320082	0,388364543	-3,425441649	0,000613801	0,010177337	REACTOME_DNA_REPAIR [332]
PTTG1	ENSG00000164611	2092,055002	-1,311532721	0,195952716	-6,693108159	2,1848E-11	9,23032E-09	GOBP_DNA_REPAIR [569]
CCNA2	ENSG00000145386	2017,460861	-1,280223222	0,584722995	-2,189452498	0,028563967	0,180154541	REACTOME_DNA_REPAIR [332]
RAD54L	ENSG00000085999	95,30515172	-1,264984213	0,41289	-3,063731777	0,002185948	0,028823949	KEGG_HOMOLOGOUS_RECOMBINATION [28]
RMI2	ENSG00000175643	198,7630434	-1,256125997	0,317193169	-3,96012941	7,49092E-05	0,002013207	REACTOME_DNA_REPAIR [332]
EME1	ENSG00000154920	125,8010331	-1,251873356	0,378354632	-3,308730094	0,000937201	0,014493003	KEGG_HOMOLOGOUS_RECOMBINATION [28]
HMGB2	ENSG00000164104	2568,528678	-1,247776619	0,623843451	-2,000143812	0,045484737	0,242631208	GOBP_DNA_REPAIR [569]
H4C1	ENSG00000278637	384,8643662	-1,239926814	0,314814741	-3,938591977	8,19612E-05	0,002148074	REACTOME_DNA_REPAIR [332]
BLM	ENSG00000197299	392,269428	-1,238186534	0,264789399	-4,676118227	2,92356E-06	0,000142957	KEGG_HOMOLOGOUS_RECOMBINATION [28]
PIF1	ENSG00000140451	89,12425074	-1,225055521	0,430923506	-2,842860752	0,00447106	0,049708774	GOBP_DNA_REPAIR [569]
H2AX	ENSG00000188486	1633,516624	-1,214070301	0,226237375	-5,366356033	8,03433E-08	7,50961E-06	REACTOME_DNA_REPAIR [332]
MCM2	ENSG00000073111	1471,107745	-1,212075792	0,212945245	-5,691959872	1,25589E-08	1,72269E-06	GOBP_DNA_REPAIR [569]
PCLAF	ENSG00000166803	400,8196156	-1,211648027	0,262104055	-4,622774828	3,78641E-06	0,000178536	REACTOME_DNA_REPAIR [332]
GINS2	ENSG00000131153	692,4481938	-1,198244536	0,216352556	-5,538388641	3,05267E-08	3,62273E-06	GOBP_DNA_REPAIR [569]
CHAF1B	ENSG00000159259	475,6941015	-1,192518656	0,27551539	-4,328319574	1,50251E-05	0,000547535	GOBP_DNA_REPAIR [569]
MCM7	ENSG00000166508	3970,843886	-1,192254667	0,206152086	-5,78337426	7,32169E-09	1,14107E-06	GOBP_DNA_REPAIR [569]
MCM3	ENSG00000112118	2961,430599	-1,179418929	0,179290935	-6,57824071	4,76047E-11	1,7338E-08	GOBP_DNA_REPAIR [569]
POLE2	ENSG00000100479	114,5677156	-1,155770914	0,393054504	-2,940485102	0,003276988	0,039064947	KEGG_BASE_EXCISION_REPAIR [35]
H2BC7	ENSG00000277224	244,6185528	-1,153603703	0,356981821	-3,231547476	0,001231219	0,018061294	REACTOME_DNA_REPAIR [332]
FANCA	ENSG00000187741	276,1320378	-1,147377048	0,323144533	-3,550662107	0,000384263	0,007145405	REACTOME_DNA_REPAIR [332]
ESCO2	ENSG00000171320	604,1535975	-1,131052097	0,254374819	-4,446399614	8,73214E-06	0,000354727	GOBP_DNA_REPAIR [569]
CHAF1A	ENSG00000167670	652,2068713	-1,126431655	0,225719477	-4,990405206	6,02528E-07	3,97744E-05	GOBP_DNA_REPAIR [569]
MCM4	ENSG00000104738	3502,112152	-1,118147714	0,178359277	-6,269075182	3,63199E-10	9,35635E-08	GOBP_DNA_REPAIR [569]
HMGB1	ENSG00000189403	4022,455871	-1,097626305	0,161937686	-6,778078246	1,21785E-11	5,59257E-09	KEGG_BASE_EXCISION_REPAIR [35]
BRCA2	ENSG00000139618	475,1108442	-1,095058696	0,230034854	-4,760403373	1,93206E-06	0,000103063	KEGG_HOMOLOGOUS_RECOMBINATION [28]
DTL	ENSG00000143476	1403,11263	-1,074765995	0,192323372	-5,588327526	2,29267E-08	2,98953E-06	REACTOME_DNA_REPAIR [332]
MCM5	ENSG00000100297	1618,342543	-1,072958858	0,202528225	-5,297823822	1,17191E-07	1,01457E-05	GOBP_DNA_REPAIR [569]
MCM6	ENSG00000076003	1350,168882	-1,070443972	0,191730505	-5,583065521	2,36316E-08	3,04386E-06	GOBP_DNA_REPAIR [569]
XRCC3	ENSG00000126215	153,407276	-1,067855756	0,409861183	-2,605408369	0,009176482	0,083650383	KEGG_HOMOLOGOUS_RECOMBINATION [28]
PAXX	ENSG00000148362	273,4354076	-1,066297861	0,285542718	-3,734284907	0,000188249	0,004057733	GOBP_DNA_REPAIR [569]
ZWINT	ENSG00000122952	1208,569743	-1,057468524	0,216065679	-4,894199437	9,87067E-07	6,06128E-05	HALLMARK_DNA_REPAIR [150]
H2BU1	ENSG00000196890	164,4035717	-1,0526433	0,425867637	-2,471761665	0,013444912	0,107579665	REACTOME_DNA_REPAIR [332]
DDX11	ENSG00000013573	451,5202913	-1,051661549	0,247909922	-4,24211158	2,21427E-05	0,000754422	GOBP_DNA_REPAIR [569]
H2AZ1	ENSG00000164032	7719,34297	-1,050492077	0,167503262	-6,271472355	3,5765E-10	9,35635E-08	REACTOME_DNA_REPAIR [332]
TRIP13	ENSG00000071539	869,8179167	-1,046154634	0,226576705	-4,617220622	3,88914E-06	0,000182389	GOBP_DNA_REPAIR [569]
RAD51	ENSG00000051180	257,3393749	-1,029007726	0,300546848	-3,423784787	0,000617555	0,010223537	HALLMARK_DNA_REPAIR [150]
DNA2	ENSG00000138346	657,8128943	-1,018641876	0,215024678	-4,737325439	2,16557E-06	0,000112121	REACTOME_DNA_REPAIR [332]
UBE2T	ENSG00000077152	667,2240543	-1,00051634	0,248650561	-4,023784771	5,72703E-05	0,001617349	REACTOME_DNA_REPAIR [332]
CLSPN	ENSG00000092853	757,2423379	-0,999979178	0,221806732	-4,508335558	6,53382E-06	0,000289959	REACTOME_DNA_REPAIR [332]
FANCD2	ENSG00000144554	846,2549826	-0,990211718	0,201856287	-4,905528246	9,31762E-07	5,78898E-05	REACTOME_DNA_REPAIR [332]
POLA1	ENSG00000101868	675,0218176	-0,984358017	0,20494672	-4,802994741	1,5631E-06	8,6437E-05	HALLMARK_DNA_REPAIR [150]
MCM8	ENSG00000125885	296,7887492	-0,977502892	0,267888176	-3,648921385	0,000263344	0,005247992	GOBP_DNA_REPAIR [569]
RMI1	ENSG00000178966	149,590574	-0,973469008	0,363808538	-2,675772851	0,007455716	0,072645083	REACTOME_DNA_REPAIR [332]
BRCA1	ENSG00000012048	987,4511882	-0,970000371	0,189075516	-5,130227294	2,89393E-07	2,12261E-05	REACTOME_DNA_REPAIR [332]

Extended Data Table 1